On the footprint of anisotropy on isotropic full waveform inversion: the Valhall case study

Vincent Prieux, Romain Brossier, Yaser Gholami, Stéphane Operto, Jean Virieux, O.I. Barkved, J.H. Kommedal

Geophysical Journal International

Geophys. J. Int. (2011) **187,** 1495–1515 doi: 10.1111/j.1365-246X.2011.05209.x

On the footprint of anisotropy on isotropic full waveform inversion: the Valhall case study

Vincent Prieux,[1] Romain Brossier,[2] Yaser Gholami,[1] Stéphane Operto,[3] Jean Virieux,[2] O. I. Barkved[4] and J. H. Kommedal[4]

[1] *Géoazur, Université Nice-Sophia Antipolis, CNRS, IRD, Observatoire de la Côte d'Azur, Valbonne, France.*
[2] *ISTerre, Observatoire des Sciences de l'Univers de Grenoble, Université Joseph Fourier, BP 53, 38041 Grenoble, Cedex 9, France.*
[3] *Géoazur, Université Nice-Sophia Antipolis, CNRS, IRD, Observatoire de la Côte d'Azur, Villefranche-sur-mer, France. E-mail: operto@geoazur.obs-vlfr.fr*
[4] *BP Norge, Stavanger, Norway*

Accepted 2011 August 26. Received 2011 August 3; in original form 2011 March 28

SUMMARY

The validity of isotropic approximation to perform acoustic full waveform inversion (FWI) of real wide-aperture anisotropic data can be questioned due to the intrinsic kinematic inconsistency between short- and large-aperture components of the data. This inconsistency is mainly related to the differences between the vertical and horizontal velocities in vertical-transverse isotropic (VTI) media. The footprint of VTI anisotropy on 2-D acoustic isotropic FWI is illustrated on a hydrophone data set of an ocean-bottom cable that was collected over the Valhall field in the North Sea. Multiscale FWI is implemented in the frequency domain by hierarchical inversions of increasing frequencies and decreasing aperture angles. The FWI models are appraised by local comparison with well information, seismic modelling, reverse-time migration (RTM) and source-wavelet estimation. A smooth initial VTI model parameterized by the vertical velocity V_0 and the Thomsen parameters δ and ϵ were previously developed by anisotropic reflection traveltime tomography. The normal moveout ($V_{\mathrm{NMO}} = V_0\sqrt{1+2\delta}$) and horizontal ($V_{\mathrm{h}} = V_0\sqrt{1+2\epsilon}$) velocity models were inferred from the anisotropic models to perform isotropic FWI. The V_{NMO} models allows for an accurate match of short-spread reflection traveltimes, whereas the V_{h} model, after updating by first-arrival traveltime tomography (FATT), allows for an accurate match of first-arrival traveltimes. Ray tracing in the velocity models shows that the first 1.5 km of the medium are sampled by both diving waves and reflections, whereas the deeper structure at the reservoir level is mainly controlled by short-spread reflections. Starting from the initial anisotropic model and keeping fixed δ and ϵ models, anisotropic FWI allows us to build a vertical velocity model that matches reasonably well the well-log velocities. Isotropic FWI is performed using either the NMO model or the FATT model as initial model. In both cases, horizontal velocities are mainly reconstructed in the first 1.5 km of the medium. This suggests that the wide-aperture components of the data have a dominant control on the velocity estimation at these depths. These high velocities in the upper structure lead to low values of velocity in the underlying gas layers (either equal or lower than vertical velocities of the well log), and/or a vertical stretching of the structure at the reservoir level below the gas. This bias in the gas velocities and the mispositioning in depth of the deep reflectors, also shown in the RTM images, are required to match the deep reflections in the isotropic approximation and highlight the footprint of anisotropy in the isotropic FWI of long-offset data. Despite the significant differences between the anisotropic and isotropic FWI models, each of these models produce a nearly-equivalent match of the data, which highlights the ill-posedness of acoustic anisotropic FWI. Hence, we conclude with the importance of considering anisotropy in FWI of wide-aperture data to avoid bias in the velocity reconstructions and mispositioning in depth of reflectors. Designing a suitable parameterization of the VTI acoustic FWI is a central issue to manage the ill-posedness of the FWI.

Key words: Inverse theory; Controlled source seismology; Seismic anisotropy; Seismic tomography; Computational seismology; Wave propagation.

INTRODUCTION

Full waveform inversion (FWI) is a multiscale data-fitting approach for velocity-model building from wide-aperture/wide-azimuth acquisition geometries (Pratt 1999). Since the pioneering works on FWI in the eighties (Gauthier *et al.* 1986; Mora 1987, 1988; Neves & Singh 1996), the benefits of wide apertures or long offsets to reconstruct long and intermediate wavelengths of a medium, and hence, to improve FWI resolution, have been recognized. In the framework of frequency-domain FWI, Pratt & Worthington (1990); Pratt *et al.* (1996); Pratt (1999); Sirgue & Pratt (2004) also show how the redundant wavenumber coverage provided by wide-aperture surveys can be taken advantage of in the design of efficient FWI algorithms, as applied to decimated data sets that correspond to a few discrete frequencies. On the other hand, wide apertures and long offsets increase the non-linearity of the inversion, because the wave fronts integrate the medium complexity over many propagated wavelengths, and then make the local optimization subject to cycle-skipping artefacts (Sirgue 2006; Pratt 2008). Cycle skipping artefacts will arise when the relative traveltime error, namely, the ratio between the traveltime error and the duration of the simulation, exceeds half of the inverse of the number of propagated wavelengths (Pratt 2008; Virieux & Operto 2009). The most efficient approach to mitigate these non-linearities consists of the recording and inverting of sufficiently low frequencies. For typical hydrocarbon exploration surveys with a few kilometres penetration depth, maximum recording distances 10–20 km and maximum recording times 10–20 s, these frequencies can be as low as 1.5–2 Hz, and correspond to few propagated wavelengths (Plessix 2009; Plessix *et al.* 2010; Plessix & Perkins 2010). These quite low frequencies can allow the FWI to be started from a crude laterally-homogeneous initial model (Plessix *et al.* 2010). Alternatively, several multiscale strategies have been proposed to mitigate the non-linearity of the FWI. The most usual one consists of hierarchical inversions of sub-datasets of increasing high-frequency content (Bunks *et al.* 1995). In the frequency-domain, these sub-datasets generally correspond to a few discrete frequencies, which are inverted sequentially from the lower frequencies to the higher frequencies (e.g. Ravaut *et al.* 2004; Sirgue & Pratt 2004; Operto *et al.* 2006; Jaiswal *et al.* 2009). A second level of multiscaling can be implemented by hierarchical inversions of decreasing aperture angles through time damping (Brenders & Pratt 2007; Brossier *et al.* 2009a; Shin & Ha 2009) or double beam-forming (Brossier & Roux 2011), or by using offset windows in the framework of layer-stripping approaches (Shipp & Singh 2002; Wang & Rao 2009).

Most of the recent applications of FWI to real wide-aperture data have been performed in isotropic acoustic approximations, where only the reconstruction of the *P*-wave velocity is sought (e.g. Ravaut *et al.* 2004; Operto *et al.* 2006; Bleibinhaus *et al.* 2007; Jaiswal *et al.* 2009). In this framework, it is possible to question the real meaning of the reconstructed velocity, and therefore, of the validity of the isotropic approximation for the inversion of wide-aperture data, which potentially contain a significant footprint of anisotropy. An analysis of this footprint is presented by Pratt & Sams (1996), who apply isotropic and anisotropic first-arrival traveltime tomography (FATT) to cross-hole data recorded in a fractured, highly-layered medium. They show the need to incorporate anisotropic effects into the tomography, to reconcile cross-hole seismic velocities with well information. A FWI case study is also presented by Pratt *et al.* (2001), who show that isotropic and anisotropic FWI of cross-hole data allow them to match the data equally well. However, the anisotropic velocity model is significantly smoother than its isotropic counterpart, which suggests some layer-induced extrinsic anisotropy in the isotropic reconstruction. More recent case studies of mono-parameter anisotropic FWI are briefly presented by Plessix & Perkins (2010) and Vigh *et al.* (2010).

In this study, we have addressed the validity of the isotropic approximation in the framework of FWI of surface wide-aperture data through a case study of real data from the Valhall field in the North Sea. This case study clearly highlights the footprint of vertical-transverse isotropic (VTI) anisotropy on the velocity reconstruction performed by isotropic FWI of the wide-aperture data.

The Valhall oilfield in the North Sea is characterized by the presence of gas, which hampers the imaging of the reflectors at the oil-reservoir level, and by a significant VTI anisotropy (Kommedal *et al.* 2004). 3-D acoustic isotropic FWI has been applied to ocean-bottom cable (OBC) data by Sirgue *et al.* (2009, 2010). The resulting velocity model shows a series of complex channels at a depth of 150 m, and it reaches a resolution that allows it to distinguish details like fractures filled with gas at a depth of 1000 m (Fig. 1b). Using the FWI velocity model as the background model improves the migrated images of the reservoir at around a depth of 2500 m, and the overburden. Although the 3-D FWI shows impressive results, Sirgue *et al.* (2010) question the meaning of the isotropic velocities, as anisotropy is well acknowledged in the Valhall zone. The isotropic approximation should be acceptable if the medium is quasi-elliptic [low values of the η parameter (Thomsen 1986)] and if the lateral velocity contrasts are smooth enough. If these conditions are satisfied, the main effects of the anisotropy in the isotropic FWI models should be a vertical stretching of the velocity structure. The meaning of the isotropic velocity reconstructed from anisotropic wide-aperture data needs, however, to be clarified. These isotropic velocities can be steered towards horizontal, normal-moveout or vertical velocities depending on the local angular coverage provided by the acquisition geometry. This is the question we want to address in this present study by comparing the FWI velocity models inferred by 2-D anisotropic and isotropic FWI of wide-aperture data. For this, we design a complete FWI workflow with *a posteriori* model appraisal based upon reverse time migration (RTM), seismic modelling and source-wavelet estimation.

In the next section, we briefly review the main features of the FWI that we use. Then, we present the application of this imaging technique to the Valhall data set. Here, we first provide an interpretation of the main arrivals recorded in the OBC receiver gathers. Secondly, we discuss the accuracy of the possible initial velocity models for isotropic FWI of wide-aperture data; namely, the normal moveout (NMO) and horizontal velocity models. Then, we present the results of the anisotropic and isotropic FWI, where in the latter case, different initial models and data pre-conditioning are tested. Some bias in the isotropic FWI models is discussed based on the comparison of the FWI results with a vertical-seismic-profiling (VSP) log that is available for the profile, and the results of anisotropic and isotropic RTM. Before concluding, we discuss the ill-posedness of FWI, in terms of the non-unicity of the solution by comparing the data fit and the source wavelets obtained by anisotropic and isotropic FWI.

METHODS

In this study, isotropic and anisotropic acoustic FWI is performed in the frequency domain using the elastic FWI method described by Brossier (2011). The modelling engine was extended to VTI media by Brossier *et al.* (2010a). The VTI acoustic approximation is considered by setting the shear-wave velocity on the symmetry axis to

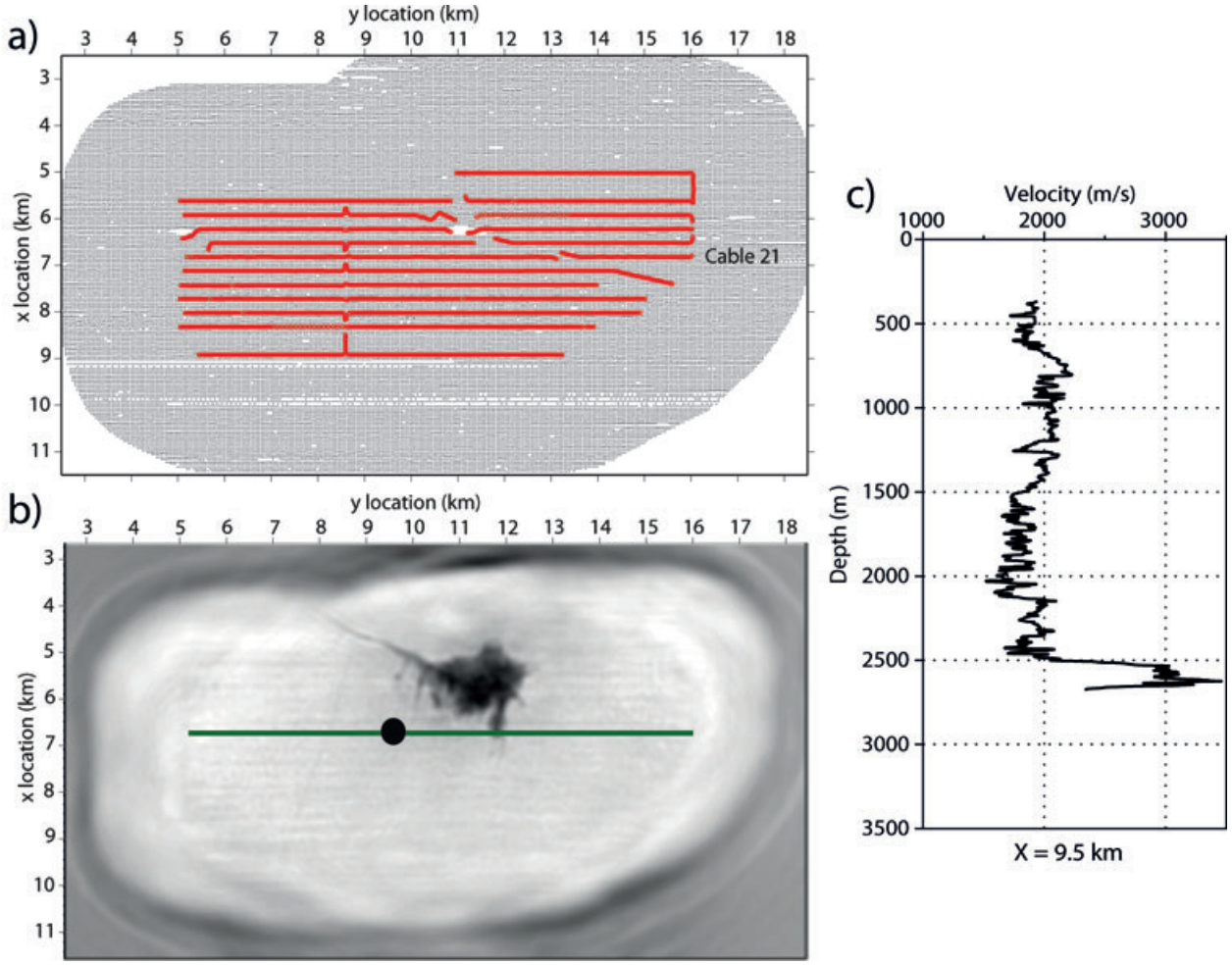

Figure 1. The Valhall experiment. (a) Layout of the Valhall survey. Points and lines denote the positions of shots and the 4C-OBC, respectively. Cable 21 is the 2-D line considered in this study. (b) Horizontal slice at a depth of 1000 m across the gas cloud extracted from the 3D-FWI model of Sirgue *et al.* (2010) (from Sirgue *et al.* (2009)). The black line matches the position of cable 21. The black circle gives the position of the well log. (c) Vertical-velocity well log extracted at position $x = 9500$ m (courtesy of BP).

zero and the pressure wavefield is approximated by the average of the normal stresses (Brossier *et al.* 2010a). The seismic modelling is performed in the frequency domain with a velocity-stress discontinuous Galerkin (DG) method on unstructured triangular mesh, which allows for accurate positioning of the sources and receivers, and accurate parameterization of the bathymetry in the framework of the shallow-water environment of Valhall (Brossier *et al.* 2008; Brossier 2011). In the frequency domain, seismic modelling can be recast in matrix form as

$$\mathbf{Au} = \mathbf{s}, \tag{1}$$

where $\mathbf{A}$ is the sparse impedance matrix, which is also known as the forward problem operator. This depends on the frequency, the mesh geometry, the DG interpolation order of each cell and the physical properties. The monochromatic wavefield vector is denoted by $\mathbf{u}$ and contains the pressure and particle velocity components at each degree of freedom of the mesh. The source vector is denoted by $\mathbf{s}$. We solve eq. (1) with the Multifrontal Massively Parallel Sparse (MUMPS) direct solver (MUMPS-team 2009).

The inverse problem is recast as a local optimization where a norm of the data residual vector $\Delta\mathbf{d} = \mathbf{d}_{\rm obs} - \mathbf{d}_{\rm cal}(\mathbf{m})$ in the vicinity of an initial model should be minimized iteratively. The vectors $\mathbf{d}_{\rm obs}$ and $\mathbf{d}_{\rm cal}(\mathbf{m})$ denote the observed and modelled data, respectively, where $\mathbf{d}_{\rm cal}(\mathbf{m}) = \mathcal{S}\,\mathbf{u}(\mathbf{m})$, and the restriction operator $\mathcal{S}$ extracts the values of the modelled wavefield $\mathbf{u}$ at the receiver positions.

In this study, the misfit function is defined by the weighted least-absolute-value (L_1) norm of the data residual vector. We choose the L_1 norm in the data space because it has been shown to be less sensitive to noise in the framework of efficient frequency-domain FWI (Brossier *et al.* 2010b), leading us to the following definition of the misfit function,

$$\mathcal{C} = \sum_{i=1,N} |s_{d_i}\,\Delta d_i|, \tag{2}$$

where $|x| = (xx^*)^{1/2}$ and N is the dimension of the data residual vector. In eq. (2), the coefficients s_{d_i} of a diagonal weighting operator $\mathbf{W}_{\rm d}$ controls the relative weight of each element of the data residual vector. The updated model at iteration $(n+1)$ is related to the initial model [i.e., the final model of iteration (n)] and to the perturbation model $\delta\mathbf{m}^{(n)}$ by

$$\mathbf{m}^{(n+1)} = \mathbf{m}^{(n)} + \alpha^{(n)}\delta\mathbf{m}^{(n)}, \tag{3}$$

where $\alpha^{(n)}$ denotes the step length estimated by line search. Minimization of the misfit function, eq. (2), leads to the following expression of the perturbation model $\delta\mathbf{m}$

$$\delta\mathbf{m}^{(n)} = -\mathbf{B}^{(n)^{-1}}\nabla C^{(n)}, \tag{4}$$

where the operator $\mathbf{B}^{(n)}$ denotes the Hessian matrix (e.g. Tarantola 2005). In this study, we shall use only the diagonal terms of the so-called approximate Hessian matrix (i.e. the linear part of the full Hessian) damped by a pre-whitening factor (Ravaut *et al.* 2004, their eq. 15), as a pre-conditioner of the Polak & Ribière (1969) pre-conditioned conjugate-gradient method, where the diagonal terms of the approximate Hessian are aimed at correcting for geometrical spreading of the data residuals and the partial derivative wavefields. Moreover, the descent direction is steered towards smooth models by filtering out the high-wavenumber components of the gradient by 2-D Gaussian smoothing (e.g. Sirgue & Pratt 2004; Ravaut *et al.* 2004; Guitton *et al.* 2010). The gradient ∇C of the misfit function C is computed using the adjoint-state method (Plessix 2006), which gives the following expression for the gradient,

$$\nabla C_{m_i} = -\Re\left\{\mathbf{u}^t \frac{\partial \mathbf{A}^{\mathrm{T}}}{\partial m_i}\bar{\lambda}\right\}, \tag{5}$$

where the real part of a complex number is denoted by $\Re$, the conjugate of a complex number by the sign $^-$, and the so-called adjoint wavefield by λ. In eq. (5), the gradient is given for one frequency and one source. The gradient that corresponds to multiple sources and frequencies is computed as the sum of the elementary gradients associated with each source–frequency couple. For the L_1 norm, the adjoint wavefield is computed by back-propagating the weighted data residuals that are normalized by their modulus (Brossier *et al.* 2010b),

$$\mathbf{A}\bar{\lambda} = \mathcal{S}^t\bar{\mathbf{r}}, \tag{6}$$

where $\bar{r}_i = s_{d_i}\overline{\Delta} d_i/|\Delta d_i|$. The operator $\partial\mathbf{A}/\partial m_i$, eq. (5), describes the radiation pattern of the virtual secondary source of the partial derivative wavefield with respect to the model parameter m_i (Pratt *et al.* 1998).

To increase the quadratic-well-posedness of the inverse problem (Chavent 2009, p. 162), the FWI algorithm is designed into a multi-scale reconstruction of the targeted medium (Brossier *et al.* 2009a; Brossier 2011). The first level of multiscaling is controlled by the outer loop over the frequency groups, where a frequency group defines a subset of simultaneously-inverted frequencies. The multi-scale algorithm proceeds over frequency groups of higher-frequency content, with possible overlap between frequency groups. A second level of multiscaling is implemented within a second loop over exponential time-damping applied from the first-arrival times t_0. The time-damping is implemented in the frequency domain by means of complex-valued frequencies, where the imaginary part of the frequency controls the amount of damping (Brenders & Pratt 2007; Brossier *et al.* 2009a; Shin & Ha 2009). A damped wavefield $\mathbf{u}$ can be written in the frequency domain as

$$\mathbf{u}\left(\omega + \frac{i}{\tau}\right)\mathrm{e}^{\frac{t_0}{\tau}} = \int_{-\infty}^{+\infty} \mathbf{u}(t)\mathrm{e}^{-\frac{(t-t_0)}{\tau}}\mathrm{e}^{\mathrm{i}\omega t}\mathrm{d}t, \tag{7}$$

where τ is the time-damping factor (s). The time-damping pre-conditioning injects in progressively more data during one frequency-group inversion: specifically shorter-aperture seismic arrivals are progressively involved as the time-damping factor τ increases. During the early stages of the frequency-group inversion, the early-arriving phases are mainly used to favour the long-wavelength reconstructions in the framework of the multiscale imaging (Sheng *et al.* 2006). Frequency-domain FWI algorithms based upon the two loops over the real part and the imaginary parts of the frequency domain were also referred to as Fourier–Laplace inversion by Shin & Ha (2009).

In real-data application, the source-wavelet signature $s(\omega)$ is generally unknown, and so it must be estimated for each frequency. As the source is linearly related to the wavefield (see eq. 1), the source-wavelet signature can be estimated by solving a least-squares linear inverse problem, assuming that the medium is known. Following Pratt (1999), we reconstructed the source function s in the frequency domain through the expression

$$s(\omega) = \frac{\mathbf{g}_{\mathrm{cal}}(\omega)^{\mathrm{T}}\mathbf{d}^*_{\mathrm{obs}}(\omega)}{\mathbf{g}_{\mathrm{cal}}(\omega)^{\mathrm{T}}\mathbf{g}^*_{\mathrm{cal}}(\omega)}, \tag{8}$$

where $\mathbf{g}_{\mathrm{cal}}$ denotes the Green functions at the receiver positions through the relationship $\mathbf{d}_{\mathrm{cal}}(\omega) = s(\omega)\mathbf{g}_{\mathrm{cal}}(\omega)$. In the framework of the adjoint-state method, for consistency with the model update performed with an L_1 norm minimization, the source signature can also be estimated alternatively with an L_1 norm minimization (R.-E. Plessix, personal communication, 2010). Such optimization has been implemented with a non-linear optimization scheme based on the very fast simulated annealing (VFSA). Our experience with source-wavelet estimation shows that for both synthetic and real data sets, non-linear L_1 and linear L_2 optimizations give similar results. The source signatures are updated for each source gather at each iteration once the incident Green functions $\mathbf{g}_{\mathrm{cal}}$ are computed, and they are subsequently used for the gradient computation and model update.

APPLICATION TO VALHALL

Geological context and acquisition geometry

Geological context

The Valhall oilfield in the North Sea has been producing oil since 1982. This is a shallow-water environment (water depth 70 m) that is located in the central zone of an old Triassic graben, which entered into compression during the late Cretaceous (Munns 1985). The subsequent inversion of stress orientations led to the formation of an anticlinal that now lies at a depth of 2.5 km, creating a high-velocity contrast respect to overlying layers. An extension regime occurred in the tertiary age, allowing for a thick deposit of sediments with gas trapped in some layers. In rising from the underlying Jurassic layers, oil was trapped underneath the cap rock of the anti-clinal. The oil migration reaches a peak nowadays, by means of numerous fractures that were induced by the different tectonic phases. Of note, these fluid are the cause of the high porosity preservation of the Valhall reservoir: a distinctive feature even though this field is affected by subsidence, which is likely to be due to production.

Ocean-bottom-cable (OBC) acquisition geometry and initial models

The layout of the 3-D wide-aperture/azimuth acquisition designed by the company BP is shown in Fig. 1(a), where the black points and the lines represent the locations on the sea floor of the shots at 5 m depth and of the permanent OBC-four-component arrays at around 70 m depth, respectively. One cable contains 220 4-C receivers. In this study, 2-D acoustic FWI is applied to the OBC line indicated as cable 21 in Fig. 1(a). This line corresponds to 320 shots recorded by 220 4-C receivers for a maximum offset of 13 km. This cable is located outside the gas cloud, as shown on the horizontal cross-section that was extracted at a depth of 1000 m from the 3-D FWI model of Sirgue *et al.* (2010) (Fig. 1b). A VSP log for vertical

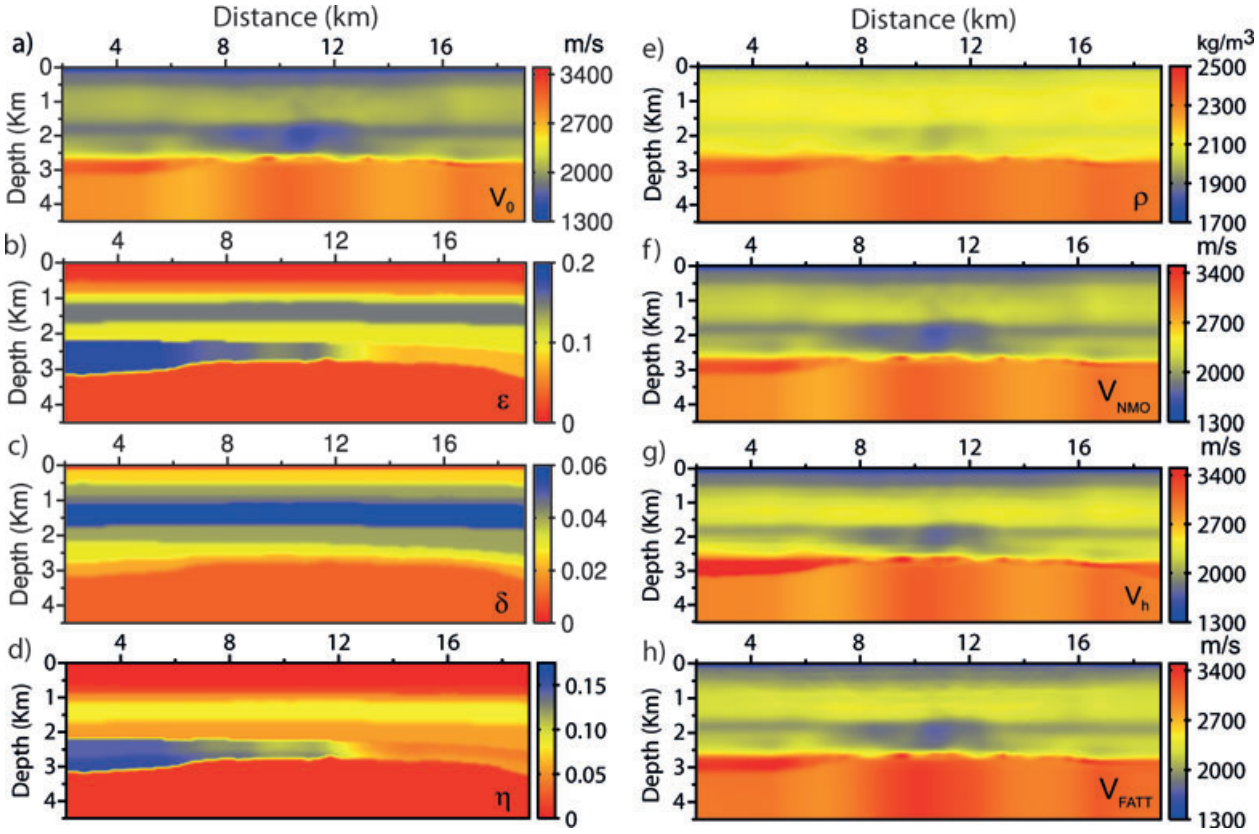

Figure 2. Two-dimensional sections along position of cable 21 through anisotropic 3-D models of the Valhall field. (a) Vertical velocity (V_0), (b) Thomsen parameter ϵ, (c) Thomsen parameter δ, (d) anellipticity parameter η, (e) density ρ, (f) NMO velocity ($V_{\rm NMO}$), (g) horizontal velocity ($V_{\rm h}$) and (h) horizontal velocity updated by the first-arrival traveltime tomography (FATT model). The V_0, δ and ϵ models were built by reflection tomography (courtesy of BP). The density model was inferred from the $V_{\rm NMO}$ model using the Gardner law.

velocity is available on line 21 and it will be used to locally assess the FWI results (Fig. 1c). A low-velocity zone that results from the presence of gas layers is clearly seen on the VSP log, between 1.5 and 2.5 km in depth.

A 3-D model for the vertical velocity V_0 and the Thomsen parameters δ and ϵ (Thomsen 1986) has been developed by anisotropic reflection traveltime tomography in VTI media, and is provided by BP (Figs 2a–c). The vertical velocity model shows the low-velocity zone associated with the gas layers between 1.5 and 2.5 km in depth, above the reservoir level (Fig. 2a). The corresponding normal moveout (NMO) and horizontal velocity models are shown in Figs 2(f–g). In this study, by NMO velocity is meant the wave speed given by $V_{\rm NMO} = V_0\sqrt{1+2\delta}$ (Tsvankin 1995), whereas the horizontal velocity is given by $V_{\rm h} = V_0\sqrt{1+2\epsilon} = V_{\rm NMO}\sqrt{1+2\eta}$, respectively, where the anellipticity coefficient η is given by $\eta = (\epsilon-\delta)/(1+2\delta)$ (Alkhalifah & Tsvankin 1995). The NMO velocities should allow the short-spread reflection traveltimes in VTI media to be matched (Tsvankin 2001), whereas the horizontal velocities should allow the refraction and long-spread reflection traveltimes to be matched. Both velocity models can be viewed as initial models of isotropic FWI of wide-aperture seismic data, as both short-aperture reflections and diving waves are recorded by long-offset acquisition and are involved in this FWI processing. The 3-D FWI model developed by Sirgue *et al.* (2010) is obtained using the NMO velocity model as the initial model (L. Sirgue, personal communication, 2010). The percentage of the anisotropy in Valhall is shown by $\eta \approx (V_{\rm h} - V_{\rm NMO})/(V_{\rm NMO})$, and it reaches a maximum value of 16 per cent (Fig. 2d).

Anatomy of the data and starting-model appraisal

A receiver gather for line 21 is shown in Fig. 3(a). The main phases that can be interpreted are as follows: (1) The first arrivals (Fig. 3a, D1, D2). The traveltime curve in the offset-time domain shows two distinct slopes with a crossover distance of around 4000 m, which suggests the presence of an interface in the upper structure, with the reflection from this interface shown in Fig. 3(a) (Rs). (2) The reflection from the top of the gas layers (Fig. 3a, Rg), which can be followed at long offsets where the traveltime curve becomes tangential to the D2 phase. (3) The reflection from the top of the reservoir at the base of the gas layers (Fig. 3a, Rr). The reflections from the top of the reservoir are disrupted at critical and supercritical distances by shingling dispersive guided waves propagated in the near surface (Fig. 3a, SW) (Robertson *et al.* 1996). These high-amplitude waves can have a harmful impact on the acoustic inversion procedure, in particular, if the sea bottom is not accurately modelled, and because they contained PS converted waves that are not accounted for by the acoustic modelling.

To validate our former interpretation and assess the kinematic accuracy of the NMO and horizontal velocity models, we compute the first-arrival traveltimes and reflection traveltimes from the top and the bottom of the gas layers using the isotropic eikonal solver of Podvin & Lecomte (1991) (Figs 3b and c). We roughly manually pick the top and the bottom of the gas layers to compute the reflection traveltimes. For a maximum offset of 11 km, the rays associated with the first-arrival traveltimes turn at a maximum depth of 1.5 km, and, therefore, they do not sample the structure at the reservoir

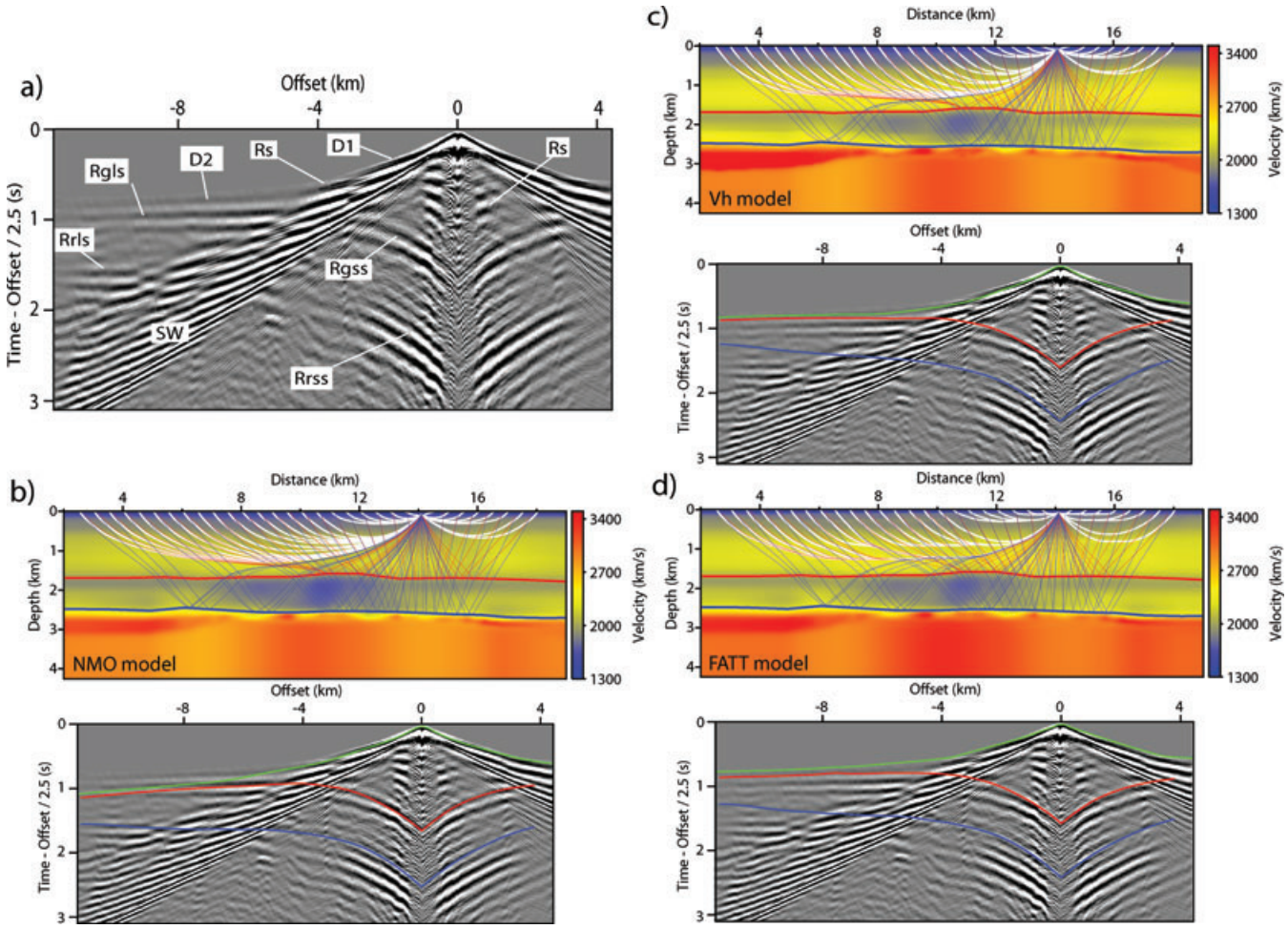

Figure 3. OBC data set. (a) Example of pre-processed recorded receiver gather, at position $x = 14\,100$ m. The vertical axis is plotted with a reduction velocity of 2.5 km s^{-1}. Phase nomenclature: D1, D2, diving waves; Rs, shallow reflection; Rgss/Rgls, short-spread and long-spread reflections from the top of the gas; Rrss/Rrls, short-spread and long-spread reflections from the top of the reservoir; SW, shingling waves. (b) Top panel: ray tracing in the NMO velocity model for the first arrival (white rays), and the reflections from the top of the gas (red) and the reservoir (blue). Top of the gas and the reservoirs are delineated by red and blue solid lines, respectively. Bottom panel: receiver gather shown in (a) with superimposed traveltime curves computed in the NMO model for these three phases. (c) As (b) for the V_h model. (d) As (c) for the FATT model. See text for details.

level below the gas layers. This implies that the first 1.5-km of the structure are constrained by both diving waves and reflected waves, whereas the deeper structure is mostly constrained by short-spread reflected waves. Superimposition of the computed traveltime curves on the receiver gather shows that the NMO velocities do not allow the traveltimes at long offsets of diving waves and the long-spread reflection Rg to be matched (Fig. 3b). The mismatch between the observed and computed first-arrival traveltimes reaches around 0.3 s at 11 km of offset. Cycle skipping artefacts will occur when this traveltime error exceeds half the period of the signal, that is for a frequency as low as roughly 1.7 Hz. In the following, we use an initial frequency of 3.5 Hz for inversion, which allows for a maximum traveltime error of 0.14 s, which is reached for an offset of the order of 6 km. We conclude that FWI might be affected by cycle skipping artefacts that result from the inversion of the diving waves and long-spread reflection recorded at offsets greater than 6 km, when the NMO velocity model is used as an initial model. In contrast, the NMO velocity model is expected to make the short-spread reflection traveltimes of the phases Rg and Rr to be matched, that is supported by Fig. 3(b). Unlike the Rg phase, the NMO velocity model reasonably predicts the slope of the long-spread reflection traveltimes of the Rr phase. Indeed, the reflection-angle illumination of the reflectors decreases with depth, which should make the reflection traveltime curve associated with the top of the reservoir less sensitive to anisotropy (i.e. the difference between vertical and horizontal velocities) within the recorded offset range. The horizontal velocity model allows for a much better agreement of the first-arrival traveltimes (Fig. 3c). The reflection traveltimes of the phase Rr computed in this model are lower than the traveltimes computed in the NMO model. The mismatch between the NMO and horizontal velocity reflection traveltimes at zero offset is of the order of 0.075 and 0.1 s for the Rg and Rr phases, respectively. Assuming that the NMO traveltimes accurately predict the observed reflection traveltimes, it is worth mentioning that these traveltime mismatches remain below the cycle-skipping limit of 0.14 s because short-offset reflection data involve fewer propagated wavelengths than long-spread reflections and diving waves. We might conclude from this analysis that the horizontal velocity model should provide a more suitable initial model than the NMO velocity model for isotropic FWI because the traveltime errors remains always below

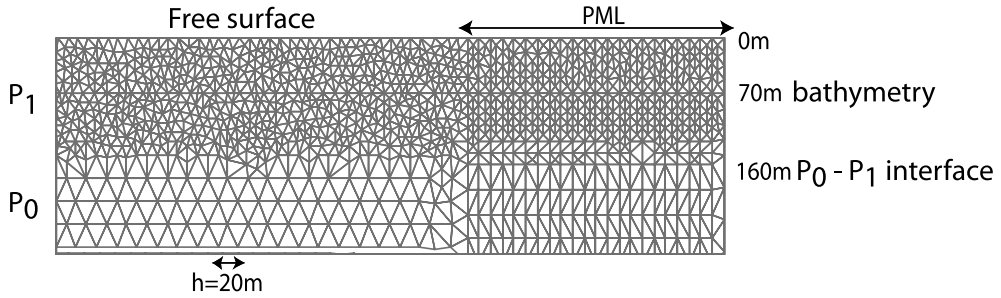

Figure 4. Seismic modelling. Close-up of the hybrid P1-P0 triangular mesh on which seismic modelling was performed using the DG method.

the cycle-skipping limit whatever the offsets. However, the NMO velocity model is expected to provide the most accurate match of the short-aperture reflection traveltimes.

The horizontal-velocity model does not accurately match the first-arrival traveltimes at intermediate offsets (with a maximum error of the order of 0.1 s at 5.5-km offset). This highlights that seismic reflection data are not suitable for accurate reconstruction of horizontal velocities. This prompted us to update the horizontal-velocity model by FATT to improve the match of the first-arrival traveltimes before FWI (Figs 2h and 3d). This updated velocity model will be referred to as the FATT model in what follows.

In continuing this study, we use the NMO model and the FATT models as initial models for isotropic FWI, and we compare the isotropic FWI models with the results of anisotropic FWI for vertical velocity.

FWI pre-processing and experimental setup

FWI pre-processing

Among the available 4-C receiver data, only the hydrophone component is considered as we are dealing with acoustic FWI. Acoustic inversion was applied to the hydrophone component of the fully elastic data computed in the synthetic elastic Valhall model (Brossier *et al.* 2009b): a successful image of the V_P structure has been obtained because converted P-SV waves have a minor footprint on the hydrophone component. Therefore, Valhall should provide a suitable framework for the successful application of acoustic FWI to elastic data (see Barnes & Charara (2009), for a more general discussion on the validity of the acoustic approximation in the marine environment). As the receivers are around 2/3-fold less numerous than the shots, the data are sorted in receiver gathers by virtue of the source–receiver reciprocity holding between an explosion source and a pressure component of the data, to reduce the computational cost.

The FWI data pre-processing first consists of minimum-phase whitening followed by Butterworth filtering of a [4–20] Hz bandwidth. The whitening is designed to preserve the geometrical spreading of the data, by normalizing the spectral amplitudes of the deconvolution operator associated with each trace according to its maximum amplitude. The bandwidth of the Butterworth filter is chosen heuristically to provide the best trade-off between the signal-to-noise ratio and the flattening of the amplitude spectrum. We then apply FK filtering to remove as much S-wave energy as possible, and spectral matrix filtering (Mari *et al.* 1999, page 386) to enhance the lateral coherency of events (Ravaut *et al.* 2004). We also applied a mute to remove noise before the first-arrival time, and after a time of 4 s following the first-arrival excluding late arrivals. Finally, the data are multiplied by the function $\sqrt{t}$ to roughly transform the 3-D geometrical spreading of real amplitude data into a 2-D amplitude behaviour. An example of a fully pre-processed receiver gather is shown in Fig. 3(a).

Experimental set-up: seismic modelling

The 18 000 × 5000 m velocity, density and attenuation models are discretized on unstructured triangular meshes for seismic modelling with the DG method, where the medium properties are piecewise constant per element (Brossier *et al.* 2008; Brossier 2011). Accurate positioning of the seismic devices is allowed by the use of a fine mesh in the first 160 m of the medium, where the linear interpolation order (P1) is used to describe the acoustic wavefield (Fig. 4). Below, a regular triangular mesh is used with piecewise-constant (P0) representation of the wavefield in each cell to reduce the cost of the modelling in terms of memory and computation. A discretization rule of 10 elements per wavelength is used in the regular mesh, which leads to 20-m-long triangle edges. The hybrid P1–P0 mesh contains around 585×10^3 cells. The mesh includes 500-m-thick perfectly matched layers on the right, left and bottom sides of the model for the absorbing boundary conditions (Berenger 1994). A free-surface boundary condition is implemented on top of the models, which implies that free-surface multiples are involved during the FWI. Although the real depth of the receivers varies between 67 and 73 m, we choose for convenience the design of a flat bathymetry at a depth of 70 m within the mesh: all receivers are put at a depth of 71 m, just below the sea bottom. This approximation has a minor impact on the modelling accuracy given the shortest propagated wavelength of 215 m.

Experimental set-up: inversion

Only the P-wave velocity is reconstructed during the inversion procedure we perform. An attenuation model is set as homogeneous below the sea bottom to the realistic value of the attenuation factor $Q_p = 150$. This value of attenuation is chosen by trial-and-error, such that the root-mean-squares amplitudes of the early-arriving phases computed in the initial model roughly matches those of the recorded data, following the approach of Pratt (1999, his Fig. 6). The density model is inferred from the starting FWI velocity models using the Gardner law (Gardner *et al.* 1974) and is kept constant over iterations of the inversion (Fig. 2e).

We sequentially invert five increasing frequency groups between 3.5 and 6.7 Hz ([3.5, 3.78, 4], [4, 4.3, 4.76], [4.76, 5, 5.25],[5.25, 5.6, 6] and [6, 6.35, 6.7] Hz). We have verified that a sufficiently high signal-to-noise ratio is inside the traces at the lowest frequency of 3.5 Hz, as already used in the 3-D FWI application of Sirgue *et al.* (2010). The spectral amplitude of the 3.5-Hz frequency represents 45 per cent of that of the dominant 7-Hz frequency after whitening

and Butterworth filtering. The maximum frequency of 6.7 Hz is similar to that used in Sirgue *et al.* (2010). We do not investigate yet whether the FWI can be pushed towards higher frequencies for this case study. We design our frequency groups with three frequencies per group, with one-frequency overlapping between the groups.

When used, the time-damping factors τ are chosen as 1, 3 and 5 s, and were applied from the first-arrival traveltime t_0. Fig. 5 shows a receiver gather where we applied various time-damping factors. When the most aggressive damping factor ($\tau = 1$ s) is applied during the early iterations of one frequency-group inversion, the inversion favours the early-arriving phases that are associated with the wide-aperture components of the data, whereas the use of higher values of τ progressively introduces later-arriving phases that are associated with shorter-aperture components.

We allow a maximum of 25 iterations within the nested loops over frequency groups and time damping (Brossier *et al.* 2009a). We note that 25 iterations are enough, because the pre-conditioned conjugate-gradient algorithm often stopped before reaching this step as we stop the iterations as soon as the maximum velocity perturbation is lower that 10^{-3} per cent of the velocity of the starting model at the position of the maximum velocity perturbation.

As the data are sorted by receiver gather for FWI, we estimate a source wavelet per receiver gather at each non-linear FWI iteration. The underlying assumption is that the shots are perfectly repetitive.

Gaussian smoothing is applied to the model velocity perturbations using horizontal and vertical correlation lengths of $0.3 \times \lambda$ and $0.1 \times \lambda$, respectively, where λ is the local wavelength. Of note, the horizontal correlation length is set three-times longer than the vertical one, as the medium is fairly tabular. The model is kept constant down to a depth of 77 m to keep the velocity in the water layer constant (above 70 m depth), and to avoid instabilities in the vicinity of the sources and receivers located at 71 and 5-m depth, respectively. No data weighting is applied during FWI, and, therefore, $\mathbf{W}_d = \mathbf{I}$, where $\mathbf{I}$ is the identity matrix.

Table 1. FWI setup used for the five applications in this study; $\mathbf{m}_0$, initial FWI model; τ(s), time damping; A/I, anisotropic versus isotropic FWI. The same frequency groups are used for each of these tests (see text).

FWI test	Anisotropic/ isotropic FWI	Initial FWI model $\mathbf{m}_0$	τ (s)
V_0 + FWI	Anisotropic	(V_0, δ, ϵ)	–
NMO+FWI	Isotropic	NMO	–
FATT+FWI 1	Isotropic	FATT	–
FATT+FWI 2	Isotropic	FATT	1, 3, 5 s
FATT+FWI 3	Isotropic	FATT	1 s

As reported by Pratt & Shipp (1999), the potential improvement in resolution provided by FWI compared to FATT, can be estimated as being of the order of $\sqrt{N_\lambda}$, where N_λ is the number of wavelengths propagating between the source and the receiver. Although we also consider starting models originally built by reflection traveltime tomography, which shows higher resolution than models built by FATT only, it might be interesting to quantify this resolution improvement. The velocities in the Valhall model range between 1500 and 3500 m s^{-1}, and FWI is performed in the 3.5–7 Hz frequency band. For a maximum offset of 13 km, it follows that FWI should lead to an increase in resolution by a factor between 4 and 8 compared to the resolution of FATT.

FWI results

We perform five applications of FWI, for which we use different approximation [isotropic versus anisotropic], starting models ((V_0,δ,ϵ), NMO, FATT models), and data pre-conditioning (without and with time dampings). The main features of the five inversion applications are outlined in Table 1.

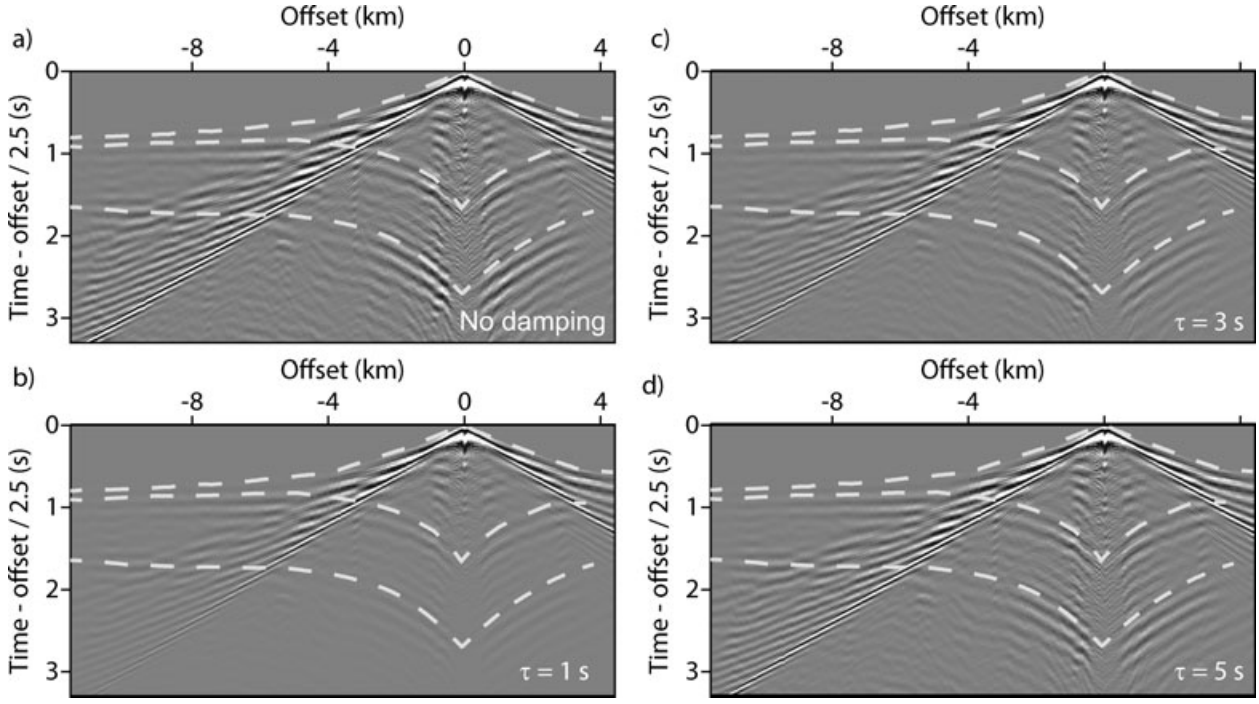

Figure 5. Data pre-conditioning according to time damping—recorded receiver gathers plotted without time damping (a), and with time damping using τ = 1 s (b), 3 s (c) and 5 s (d). The dashed lines show the first-arrival picks and the reflection picks from the top and the bottom of the gas layers.

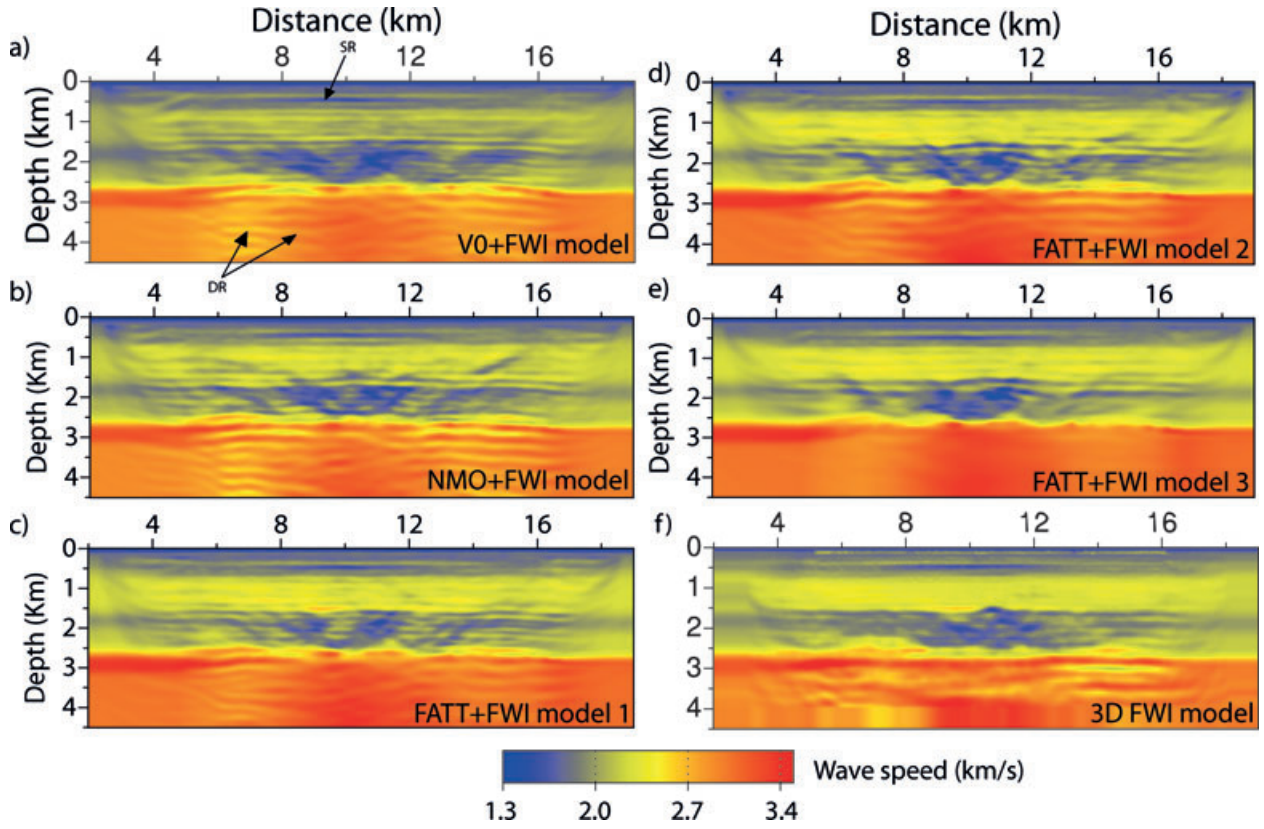

Figure 6. FWI models. (a) V_0 model built by 2-D anisotropic FWI. SR, shallow reflector at 0.6 km in depth described in the text. DR: deep reflector below the reservoir level described in the text. (b-e) FWI models built by 2-D isotropic FWI using $V_{\rm NMO}$ as the initial model (b), and using $V_{\rm FATT}$ as the initial model without (c) and with three time dampings (d) and one time damping (e) as data pre-conditioning. (f) Dip section of the 3-D FWI model of Sirgue *et al.* (2010) (courtesy of BP).

Anisotropic FWI for vertical velocity

We first perform anisotropic FWI, the results of which will be used in the following sections of this study as a reference to assess the footprint of the anisotropy on the isotropic FWI. For inversion, the VTI medium is parameterized by the vertical velocity V_0 and the Thomsen parameters δ and ϵ. Only the vertical velocity V_0 is involved in the inversion, whereas the δ and ϵ parameters are kept fixed during the inversion. The (V_0, δ, ϵ) FWI parameterization is justified because the vertical velocity has a dominant weight in the optimization process with respect to the Thomsen parameters. This allows for mono-parameter inversion as long as the background δ and ϵ models describe the large wavelengths of the medium accurately (Gholami *et al.* 2011a). This latter assumption is strongly supported because the NMO and the horizontal velocity models inferred from the initial V_0, δ, ϵ models (Fig. 2) allow the accurate matching of the short-aperture reflection and the first-arrival traveltimes, respectively (Figs 3b and c). Another benefit of (V_0, δ, ϵ) parameterization is that the diffraction pattern of the vertical velocity is isotropic for this parameterization, and therefore, it should provide a broadband reconstruction of the vertical velocity (Gholami *et al.* 2011b). Note that, when the vertical velocities are updated by mono-parameter anisotropic FWI, the horizontal velocities are updated according to the coupling between the vertical and horizontal velocities through the expression: $V_{\rm h} = V_0\sqrt{1+2\epsilon}$. Other parameterizations can be viewed that involve the elastic moduli (Lee *et al.* 2010) or the NMO velocity and η (Plessix & Cao 2011). However, a detailed discussion on the most suitable parameterization for acoustic VTI FWI is beyond the scope of this study, and this has already been discussed in Plessix & Cao (2011) and Gholami *et al.* (2011a,b).

The initial V_0 model for FWI is shown in Fig. 2(a). The background models for ϵ, δ and ρ are shown in Figs 2(b,c,e). The FWI is applied consecutively to five frequency groups without considering time damping (Test V_0 + FWI in Table 1). The final FWI model for V_0, referred to as the V_0 + FWI model in the following, is shown in Fig. 6(a). A reflector at 600 m in depth is well imaged (Fig. 6a, SR), and might be related to the reflection phase Rs in the data (Fig. 3a). This reflector is consistently reconstructed for all of the tests presented later, and therefore, it should correspond to a real feature, which will not be discussed any more in the following.

The negative velocity contrasts at the top of the gas layers at 1.5 km in depth is well delineated, and some deep reflectors below the reservoir level between 2.5 and 4 km in depth can be interpreted (Fig. 6a, DR) (see also Sirgue *et al.* 2010, their Fig. 3b). These deep reflectors are imaged with a limited wavenumber bandwidth as suggested by their vertically-oscillating nature because of the lack of low frequencies and the lack of wide aperture coverage at these depths, which prevent the reconstruction of the small wavenumbers in the deep part of the medium. At these depths, FWI performs mostly as a least-squares migration of narrow bandwidth data. Comparisons between the log of the FWI model at 9.5 km in depth and the VSP log show reasonable agreement between the two velocity profiles, in particular in the upper part down to 0.8 km in depth (Fig. 7a). The log of the FWI model remains centred on the log of the initial model, which already matches the main

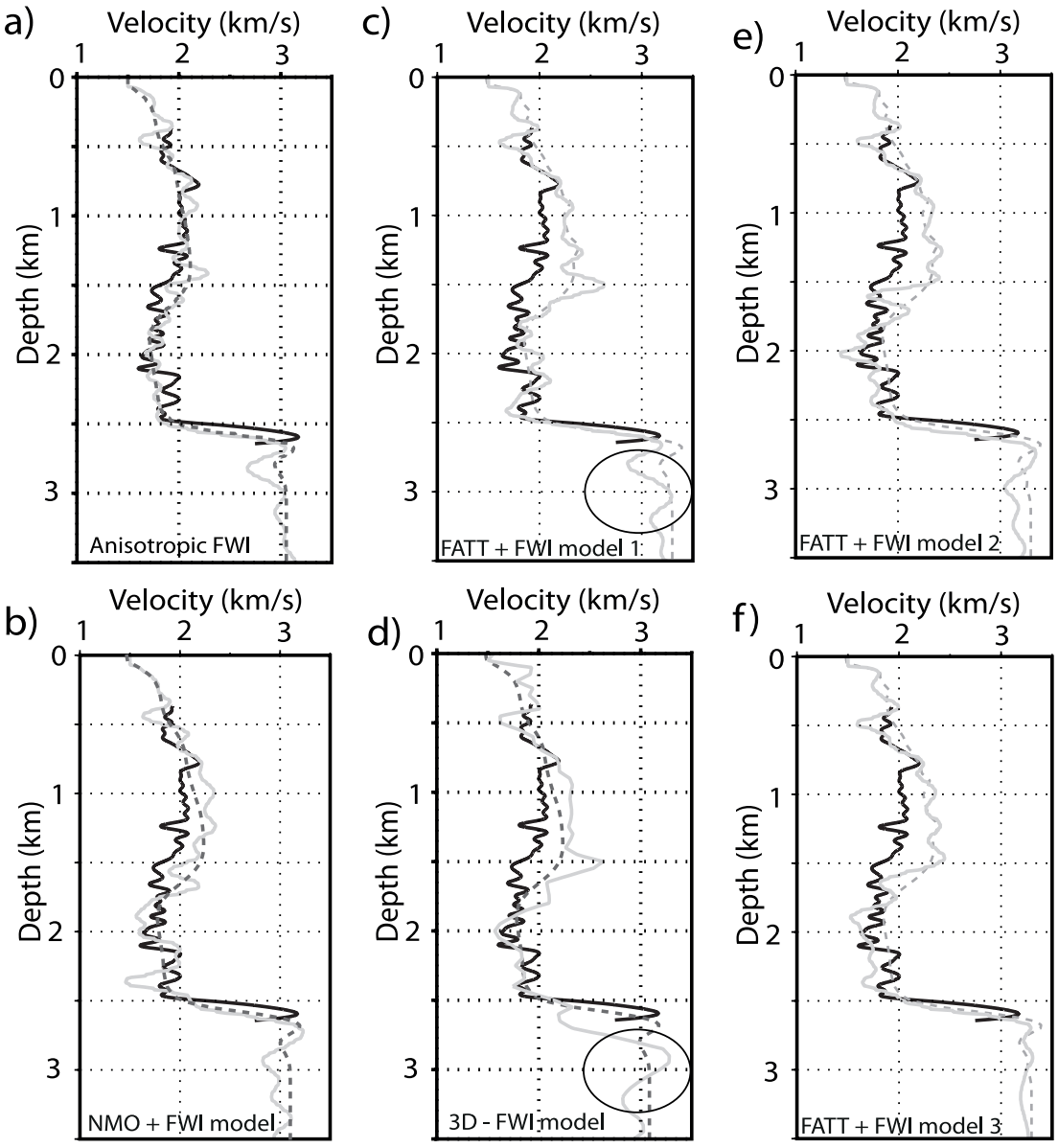

Figure 7. Log of the initial (dash grey line) and final (solid grey line) FWI models extracted at the position of the well log. The low-pass filtered well-log vertical velocities are plotted with solid black lines. (a) Anisotropic FWI. (b,c,e,f) Isotropic FWI using V_{NMO} as the initial model (b), and using V_{FATT} as the initial model for inversion tests 3 (c),4 (e),5(f) (Table 1). (d) The 3-D FWI model of Sirgue *et al.* (2010) (courtesy of BP). In (c) and (d), the deepening of the top of the reservoir, related to the stretching in depth of the velocity model, is highlighted by the black ellipses (see text for details).

trend of the VSP log quite well. Therefore, it is quite challenging to discriminate between the true features of the FWI log from the artificial ones. Rather than assessing the match of the V_0 FWI log with the VSP log in an absolute sense, we shall rather use the comparison between the V_0 + FWI log and the VSP log as a reference to highlight the differences with the isotropic FWI results presented in the following. Of note, the VSP log is low-pass filtered in the time domain after depth-to-time conversion with a cut-off frequency of 14 Hz, inferred from the theoretical vertical resolution (i.e. half a wavelength) of the FWI at the 7-Hz frequency.

Isotropic FWI using the initial NMO velocity model

We use the NMO model (Fig. 2f) as the initial model for isotropic FWI, and we invert the full data set without considering time damping, as for the anisotropic FWI (Test NMO + FWI in Table 1). The resulting FWI model, referred to as the NMO + FWI model, is shown in Fig. 6(b). The reconstructed velocities in the upper structure are clearly higher than those of the V_0 + FWI model, and are close to horizontal velocities between 0.6 and 1.4 km in depth (Fig. 7b). The reconstruction in the gas appears more unstable than in the anisotropic case, with reconstructed velocities smaller than the vertical velocities at around 2.4 km in depth. The FWI successfully images deep reflectors below the reservoir level at 3–4 km in depths with higher amplitudes than for the anisotropic FWI (Compare Figs 6a and b).

Isotropic FWI using the initial FATT velocity model

We consider now the same data pre-conditioning without time damping as for the two former tests but here we use the FATT model

as the initial model for the isotropic FWI (Test FATT + FWI 1 in Table 1). The resulting FWI model, which is referred to as the FATT + FWI model 1, is shown in Fig. 6(c). Compared to the NMO + FWI model, the FATT + FWI model 1 has slightly higher velocities between 0.6 and 1.6 km in depth, that highlights the footprint on the initial model (Fig. 7c). These velocities remained centered around the horizontal velocities of the initial model at these depths. The velocities within the gas layers between 2 and 2.5 km in depth are close to the vertical velocities along the well, and are higher than those of the NMO + FWI model. We note also a high-velocity perturbation at 3 km in depth, where the velocity reaches a maximum value of 3.3 km s^{-1} (Fig. 7b). This velocity perturbation is absent in the NMO + FWI model, where the maximum velocity is reached at a depth of 2.7 km (Fig. 7b). This deep velocity perturbation might indicate a vertical stretching of the deep structure to balance the high horizontal velocities reconstructed in the upper structure, and the velocities in the gas layers higher than those of the NMO model.

During a second test with the FATT model, we use three time dampings in cascade during the inversion of each frequency group (τ = 1, 3, 5 s) (Test FATT + FWI 2 in Table 1). Note that the wide-aperture components associated with strong time dampings are injected first during one frequency group. On one hand, this is consistent as these aperture components are those that are accurately predicted by the starting FATT model. On the other hand, this hierarchical strategy is consistent with the multiscale approach, where the long wavelengths constrained by the wide apertures must be first reconstructed. The final FWI model, referred to as FATT + FWI model 2, is shown in Fig. 6(d). As for the FATT + FWI model 1, the horizontal velocities are mainly reconstructed down to 1.5 km in depth, where the top of the gas layers is well delineated by a sharp negative velocity contrast (Fig. 7e). Overall, the velocities in the gas are lower than the vertical velocities along the well below 1.8 km in depth. The maximum velocity at the reservoir level is reached at 2.7 km in depth as for the NMO model.

During the third test performed with the FATT model, we consider only a time-damping factor of 1 s (Test FATT + FWI 3 in Table 1). A time-damping factor of 1 s favours the aperture components of the data which are well predicted by the FATT model from a kinematic viewpoint, and it heavily damps the contribution of the deep short-aperture reflections in the data. The final FWI model, referred to as FATT + FWI model 3, is shown in Fig. 6(e). The velocity structure of the FATT + FWI model 3 is similar to the one of the FATT + FWI model 2. However, the velocities in the gas are in overall lower and the deep part of the model is less perturbed and shows a smoother pattern due to the use of a more limited subdataset during inversion (compare Figs 7e and f).

For possible identification of artefacts relating to the 3-D propagation effects, we show the dip section of the 3-D isotropic FWI model of Sirgue *et al.* (2010) along cable 21 (Fig. 6f). Interestingly, the velocities above the gas between 0.5 and 1.5 km in depth are quite close to those of the FATT + FWI model 1 (compare Figs 7d and c). The vertical stretching between 2.5 and 3 km in depth of the 3-D FWI model might have a similar origin than the one hypothesized for the FATT + FWI model 1 (compare Figs 7c and d). The consistency between the dip section of the 3-D FWI model of Sirgue *et al.* (2010) and the FATT + FWI model 1 strongly supports that 3-D effects have a minor impact on the 2-D FWI results.

Model appraisals

Model appraisal is a key issue in FWI as uncertainty analysis is quite challenging to perform in a Bayesian framework (Gouveia & Scales 1998). In this study, the FWI models are evaluated based upon four criteria: the local match with the VSP log, the flatness of the common image gathers (CIG) computed by RTM, the synthetic seismogram modelling, and the repeatability of source-wavelet estimation.

Reverse time migration and common image gathers

We compute 2-D RTM and CIGs in the offset-depth domain. RTM is performed in the frequency domain using the acoustic VTI finite-difference frequency-domain modelling method of Operto *et al.* (2009) and the gradient of the FWI program of Sourbier *et al.* (2009a,b), where the data residuals are replaced by the data. Each of the common-offset migrated images was computed independently to generate CIGs before stacking. The range of offsets that is considered for migration ranges from −5 to 5 km. For migration, we use a suitable pre-processed data set, where free-surface multiples are removed. The migrated images are displayed with an automatic gain control.

The anisotropic RTM performed in the initial (V_0, δ, ϵ) model provides a good image of the subsurface, with a good continuity of the top of the reservoir beneath the gas layers at 2.5 km in depth and of a deep reflector between 3 and 3.5 km in depth (Fig. 8a, DR) (see also Fig. 3 in Sirgue *et al.* (2010)). The quality of the anisotropic migrated image is further confirmed by the overall flatness of the reflectors in the CIGs (Fig. 9a). The isotropic RTM computed in the NMO model produces an acceptable image, although the image of the top of the reservoir is slightly less focused than the one obtained by anisotropic RTM (Fig. 8b). The deep reflector below the reservoir level is shifted downwards by around 250 m with respect to its position in the anisotropic image because the NMO migration velocities in isotropic RTM are on average faster than those of anisotropic RTM when short-spread data are considered. On the other hand, the reflectors are slightly smiling in the CIGs, which suggest too slow velocities at long offsets (Fig. 9b). The migrated image computed in the FATT model shows a severe misfocusing of the top of the reservoir with a significant deepening of the deep reflector below the reservoir level, due to the high migration velocities associated with horizontal velocities (Fig. 8c). These too high velocities are clearly highlighted by frowning reflectors in the CIGs (Fig. 9c).

The migrated images computed in the FWI models are shown in Figs 8(e–h). Overall, the anisotropic FWI model does not allow us to improve the RTM image of the deep structure obtained from the anisotropic reflection traveltime tomography (compare Figs 8a and e). This is, to some extent, expected because the workflow, which combines the traveltime reflection tomography (or, migration-based velocity analysis) with the RTM, is more consistent than the one combining FWI with RTM. In the first case, the same subset of data, that is the short-spread reflections, is used during both the velocity model building and RTM, and the scale separation underlying these two tasks contributes to make the workflow well posed. In contrast, the FWI is a more ill-posed problem, where significant errors can be propagated in depth as longer offsets are processed. We note, however, that the reflectors in the CIGs inferred from the FWI model are significantly flatter in the shallow part (the first 1 km) than the ones inferred from the anisotropic reflection traveltime tomography model (Fig. 10). This highlights the capability of FWI for exploiting shallow reflections over the full aperture range, unlike reflection traveltime tomography. The improvement in the imaging of the shallow structure is observed for all of the migration tests described later. The NMO + FWI model produces CIGs, for which the smiling effects are slightly reduced (compare Figs 9b and f).

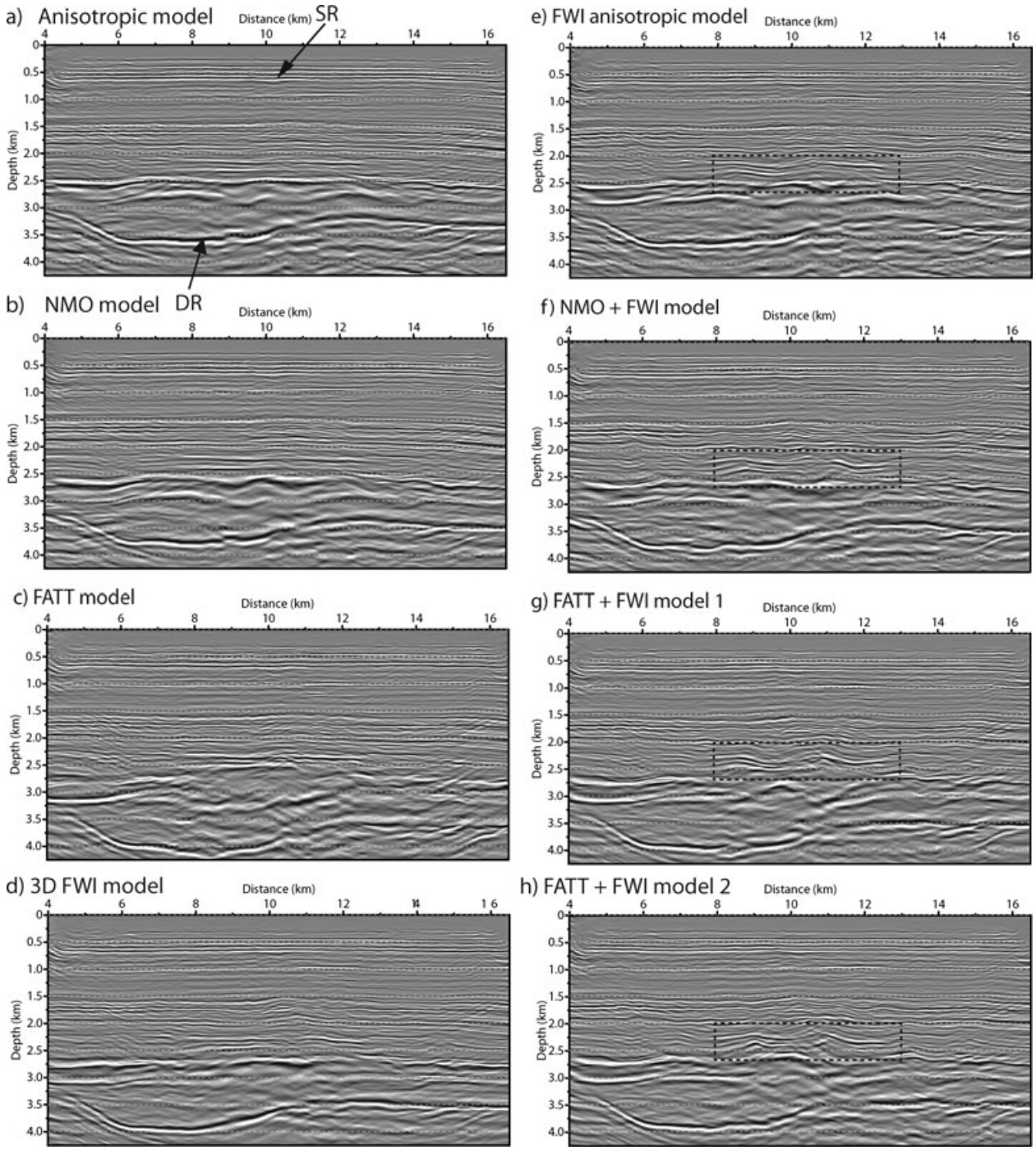

Figure 8. 2–D isotropic and anisotropic RTM images. (a–e) Anisotropic RTM images computed in the initial (a) and final (e) (V_0, δ, ϵ) FWI models. (b, f) Isotropic RTM images computed in the NMO model (b) and NMO + FWI model (f). (c,g–h) Isotropic RTM images computed in the FATT model (c) and the final FATT + FWI models 1 (g) and 2 (h). (d) Isotropic RTM image computed in the dip section of the 3-D FWI model of Sirgue *et al.* (2010). The black dashed frames in (e–h) show reflectors with suspicious horizontal undulations, which might be related to the footprint of anisotropy (see text for details).

This is consistent with the increase in the velocities shown in the NMO + FWI model compared to the NMO model. Similarly, the FATT + FWI models help to reduce the frowning effects in the CIGs inferred from the FATT model (compare Figs 9c and g–h). As expected, the RTM images inferred from the FATT and the FATT + FWI models are less well focused than the anisotropic and NMO counterparts (Fig. 8). This probably reflects the footprint of the initial FATT model, the horizontal velocities of which are not suitable for migration. However, the FATT + FWI model 2, compared to the FATT model, improves the imaging of the deep reflector that is raised by 300 m (compare Figs 8c and g–h). Note also how the deep reflector in the RTM images inferred from the FATT + FWI models is positioned at the same depths than the one inferred from the 3-D FWI model between 4 and 11 km of distance (compare the RTM images in Figs 8d, g, h and the corresponding velocity logs in Figs 7c–e).

A striking feature of the RTM images inferred from the FWI models is suspicious horizontal fluctuations of the reflectors above

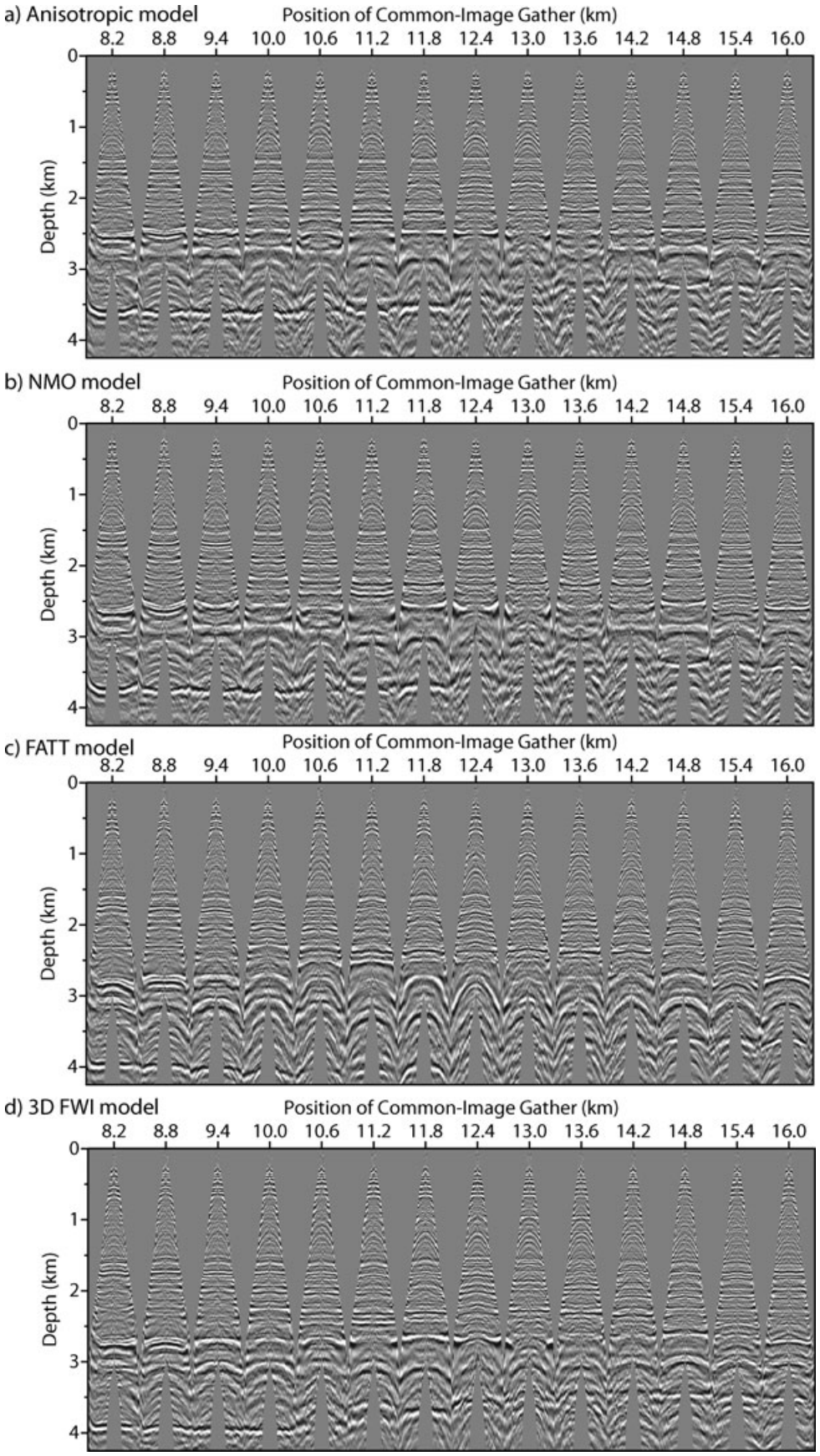

Figure 9. CIGs corresponding to RTM images of Fig. 8. The horizontal axis gives the horizontal position of the CIG. Minimum and maximum offsets are −5 and 5 km, respectively. Internal and external mutes were applied to the CIGs, which are plotted with an automatic gain control.

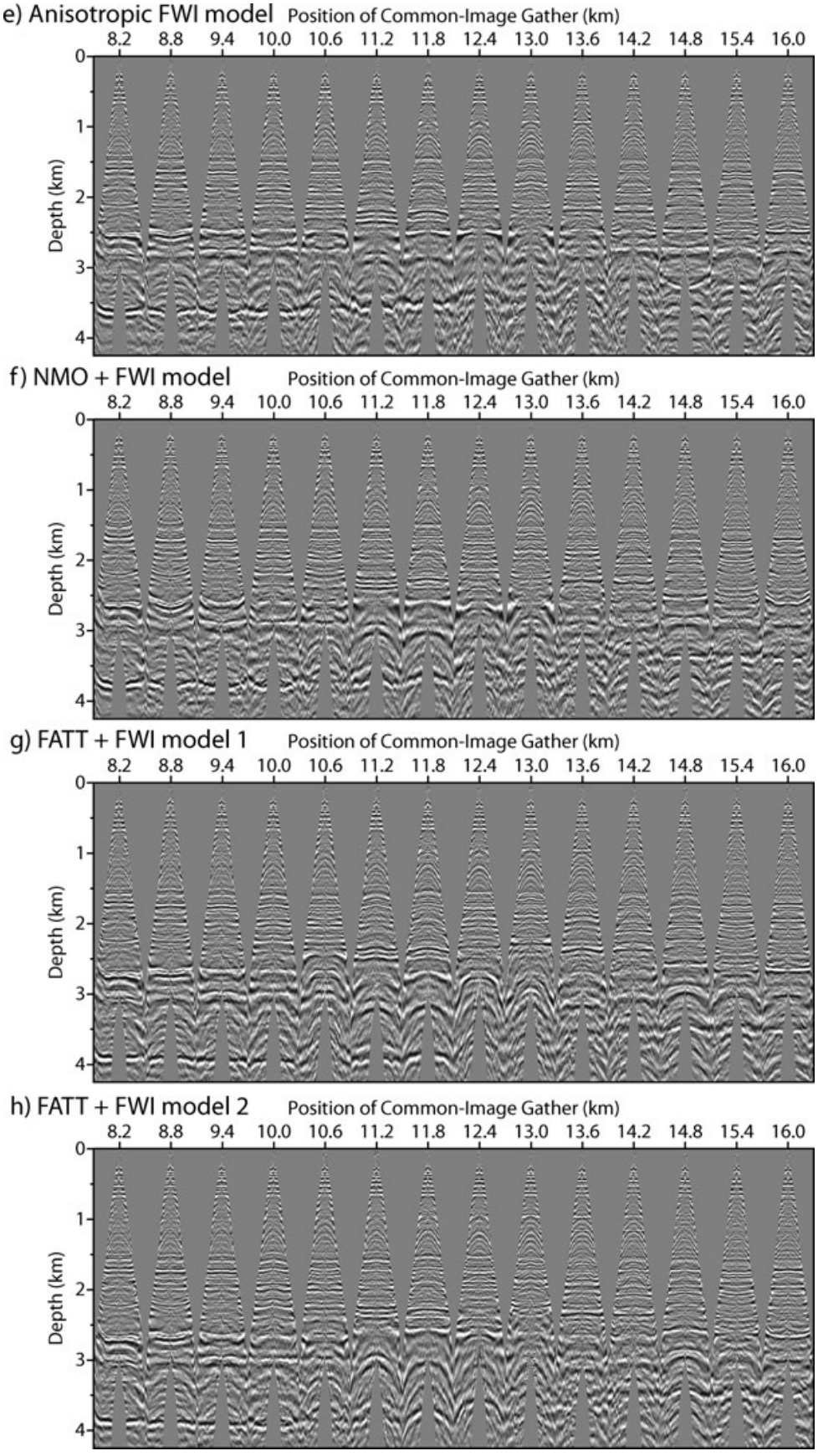

Figure 9. (*Continued.*)

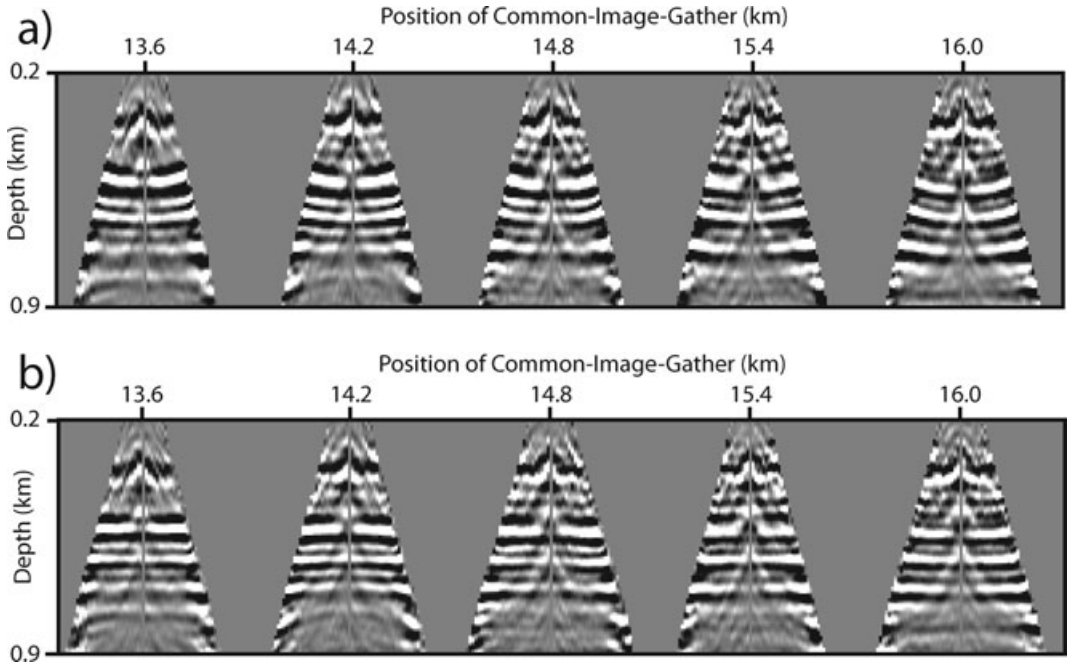

Figure 10. Close-up of the CIGs of Fig. 9a (a) and Fig. 9e (b). The five most rightward CIGs are shown down to 900 m in depth. Note how the FWI allows for the flattening of shallow events.

the reservoir level between 2 and 2.5 km in depth (Figs 8e–h). This trend appears to gradually increase from the anisotropic RTM image to the FATT + FWI model 2 RTM image (from Figs 8e to h). Although many factors might explain these fluctuations, one possible explanation would be related to the footprint of anisotropy. Indeed, the footprint of the anisotropy in the FWI results is expected to increase from the anisotropic FWI to the FATT + FWI application 2. For anisotropic FWI, the inaccuracies in the δ and ϵ background models might introduce some small bias into the V_0 + FWI model through some trade-offs between vertical velocity and ϵ. On the other hand, the time dampings used in the FATT + FWI inversion (model 2) might contribute to strengthen artefacts associated with anisotropy because conflicting subdatasets sensitive to different kinds of velocities (ranging from vertical velocities to horizontal velocities through NMO velocities) are inverted hierarchically rather than simultaneously. Indeed, degrading data redundancy during successive intermediate stages of the FWI should give more freedom to the inversion to inject in the models artificial features to accommodate anisotropic effects. These horizontal fluctuations might be related with the lateral heterogeneity of the FWI models at the base of the gas layers and on top of the reservoir, that seems to increase from the V_0 + FWI model to the FATT + FWI model 1 (Fig. 6).

Seismic modelling

For seismic modelling, we need a source wavelet, which is estimated by a VFSA method using a suitable subdataset and velocity model. We use the NMO velocity model and the first 2 km of offsets for the source estimation in the isotropic approximation. In this setting, the source-wavelet estimation is mainly controlled by the short-aperture reflection wavefield, which should be well predicted by the NMO model. The 220 sources wavelets associated with each receiver gather and the mean wavelet are shown in Fig. 11(a). The source wavelet is computed within the 4–20 Hz frequency band. With the assumption of a uniform receiver-ground coupling all along the profile (a reasonable assumption according to the lithology of the sea bed, which is composed of hard sand (Kommedal *et al.* 1997)) and a sufficiently-accurate velocity model, we should end up with quite similar source wavelets, as shown in Fig. 11(a). In the following, we use the mean wavelet shown in the right panel of Fig. 11(a) for the seismic modelling.

Fig. 12 shows a qualitative comparison between the receiver gather of Fig. 3(a) and synthetic seismograms computed in the final V_0 + FWI model (Fig. 6a) with the same DG modelling engine as for the FWI. Relatively good agreement is obtained between these two sets of seismograms, although we note underestimated amplitudes of the short-spread reflections Rg and Rs. This might be because, on one hand, it is generally acknowledged that data-space optimization by opposition to image-space optimization (or, migration-based velocity analysis) is not optimal to match short-spread reflections, (e.g. Symes 2008), and, on the other hand, we consider only a smooth model for the density, which might have led to underestimate impedance contrasts.

A direct comparison between the recorded seismograms and the isotropic and anisotropic synthetic seismograms computed in the initial and final FWI models is shown in Fig. 13. The first obvious conclusion is that the data match obtained with the final FWI models (Figs 13e–h) has been significantly improved compared to that obtained with the initial FWI models (Figs 13a–c). A second important conclusion is that the data fits achieved with the V_0 + FWI model, the NMO + FWI model, and the FATT + FWI models 1 and 2 are close, disregarding the discrepancies between these models. This thereby highlights the ill-posedness of the FWI in terms of non-unicity of the models to match anisotropic data. For all of the simulations performed in the FWI models, a reasonable match of the diving waves (D1, D2) and the reflections (Rs, Rg, Rr) has been achieved. The amplitudes of the diving waves (D1, D2) are, however, better matched in the seismograms computed in the FATT + FWI models than in the seismograms computed in the NMO + FWI model (compare Figs 13f and g–h). This probably reflects the

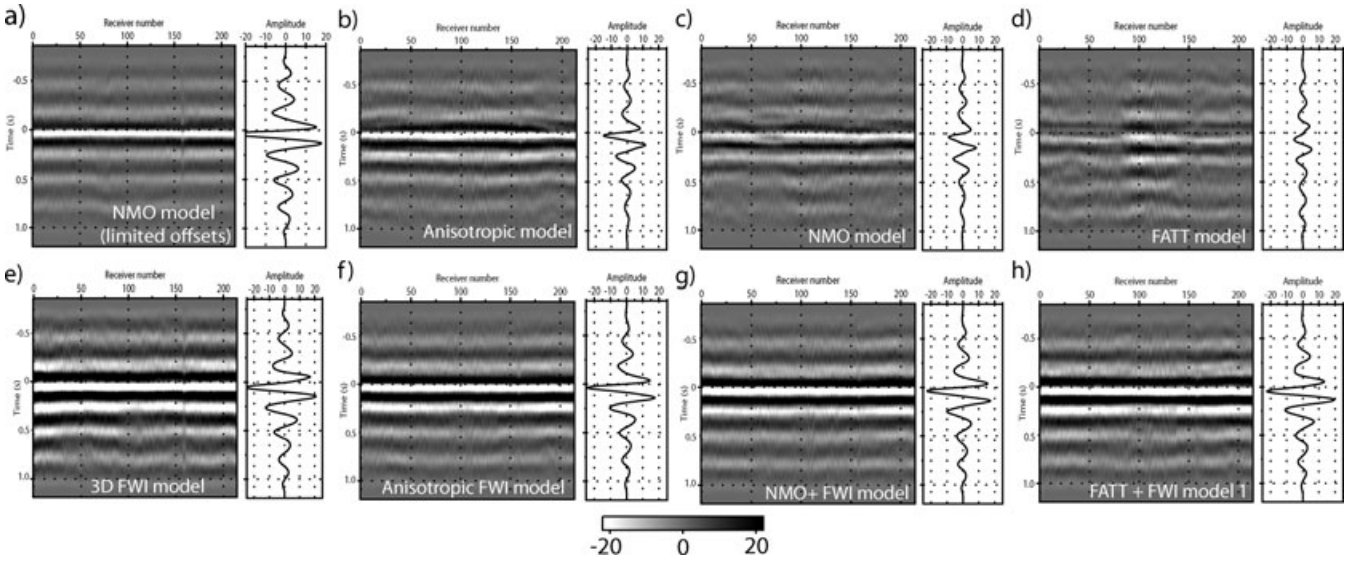

Figure 11. Source-wavelets estimation. (a) Using isotropic modeling for a maximum offset of 2 km and the NMO velocity model. (b, f) Using anisotropic modeling for the full offset range and the initial (b) and final (f) (V_0, δ, ϵ) FWI models. (c, g) Using isotropic modeling and the NMO model (c) and NMO + FWI models (g). (d, h) As (c, g) for the FATT model (d) and the FATT + FWI model 1 (h). (e) Using isotropic modeling for the full offset range and the dip section of the 3D FWI model of Sirgue *et al.* (2010). Note the improved focusing of the wavelets when using the FWI models.

kinematic accuracy of the FATT model to match first-arrival traveltimes. However, the seismograms computed in the NMO + FWI model do not show obvious evidence of cycle skipping artefacts at large offsets for the diving waves, as the first-arrival traveltimes computed in the NMO + FWI model accurately match the observed first-arrival traveltimes (Fig. 13f). The match of the first arrivals is consistent with our showing that the FWI converged towards velocities close to the horizontal velocities in the upper structure when the NMO model is used as the initial model (Fig. 7b). The successful match of the diving waves recorded at long offsets is unexpected when the NMO model is used as the initial FWI model because the traveltime mismatch between the recorded and the computed first-arrival traveltimes (0.3 s) exceeds the cycle-skipping limit at long offsets for a starting frequency of 3.5 Hz. This successful match can be interpreted on the basis that the FWI has performed a hierarchical layer-stripping reconstruction of the velocity structure over iterations, where the shallow part of the medium constrained by the high-amplitude short-offset early arrivals are reconstructed first followed by the reconstruction of the deeper part. This hierarchical reconstruction of the velocity structure according to depth might have contributed to the progressive absorption of the traveltime misfit with the offset, as the shallow part of the medium is improved by the FWI. The match of the short-spread reflection phases is almost equivalent in all of the seismograms, which is consistent with the concept that all of the initial models allow the prediction of the traveltimes within the cycle-skipping limit.

The data match is also shown by the plot of the misfit functions at the first and last FWI iterations as a function of the frequency group. The curves show essentially similar trends for the anisotropic FWI and the isotropic FWI using the NMO and FATT models as initial models (Fig. 14).

Source-wavelet estimation as a tool for model appraisal

We use the source-wavelet estimation as a tool to appraise the relevance of the FWI models (Jaiswal *et al.* 2009). We estimate the source wavelets by considering the full offset range, to make the wavelet estimation more sensitive to the model quality (Fig. 11). The sensitivity of the wavelet estimation to the amount of data used in eq. (8) can be assessed by comparing the wavelets estimated in the NMO model using maximum offsets of 2000 m (Fig. 11a) and 13 000 m (Fig. 11c). If the velocity model is not accurate enough, the repeatability of the wavelets is strongly affected when all of the aperture components of the data are involved in the inversion process. The collection of the source wavelets and the corresponding mean wavelet inferred from the initial and final FWI models when the full offset range is involved in the estimation is shown in Figs 11(b–d) and (f–h). Comparisons between the wavelets computed in the initial and the final FWI models show how the source-wavelet estimation is improved when a FWI model is used, hence validating the relevance of the FWI results. The wavelet inferred from the dip section of the 3D FWI model of Sirgue *et al.* (2010) is shown in Fig. 11(e). This has a similar shape and amplitude to that obtained by 2D FWI.

DISCUSSION

We have presented here the application of VTI anisotropic and isotropic acoustic FWI to wide-aperture OBC data from the Valhall field. We used both NMO and FATT models as initial models for the isotropic FWI, where the FATT model roughly represents the horizontal velocities of the VTI medium. The results highlight the footprint of anisotropy on isotropic FWI.

Although there are significant differences between the kinematic properties of the initial models we used, the final isotropic FWI models show some overall common features. The most obvious one is that the horizontal velocities are mainly reconstructed in the upper structure, whatever the initial model and the data pre-conditioning. Therefore, the isotropic velocities in the upper structure are significantly higher than the velocities reconstructed by the mono-parameter anisotropic FWI for the vertical velocity. The horizontal velocities are also reconstructed in the 3-D isotropic FWI model of Sirgue *et al.* (2010), and, therefore they cannot be interpreted as the footprint of the 3D effects. The reconstruction of the horizontal velocities in the upper structure shows that the FWI imaging is

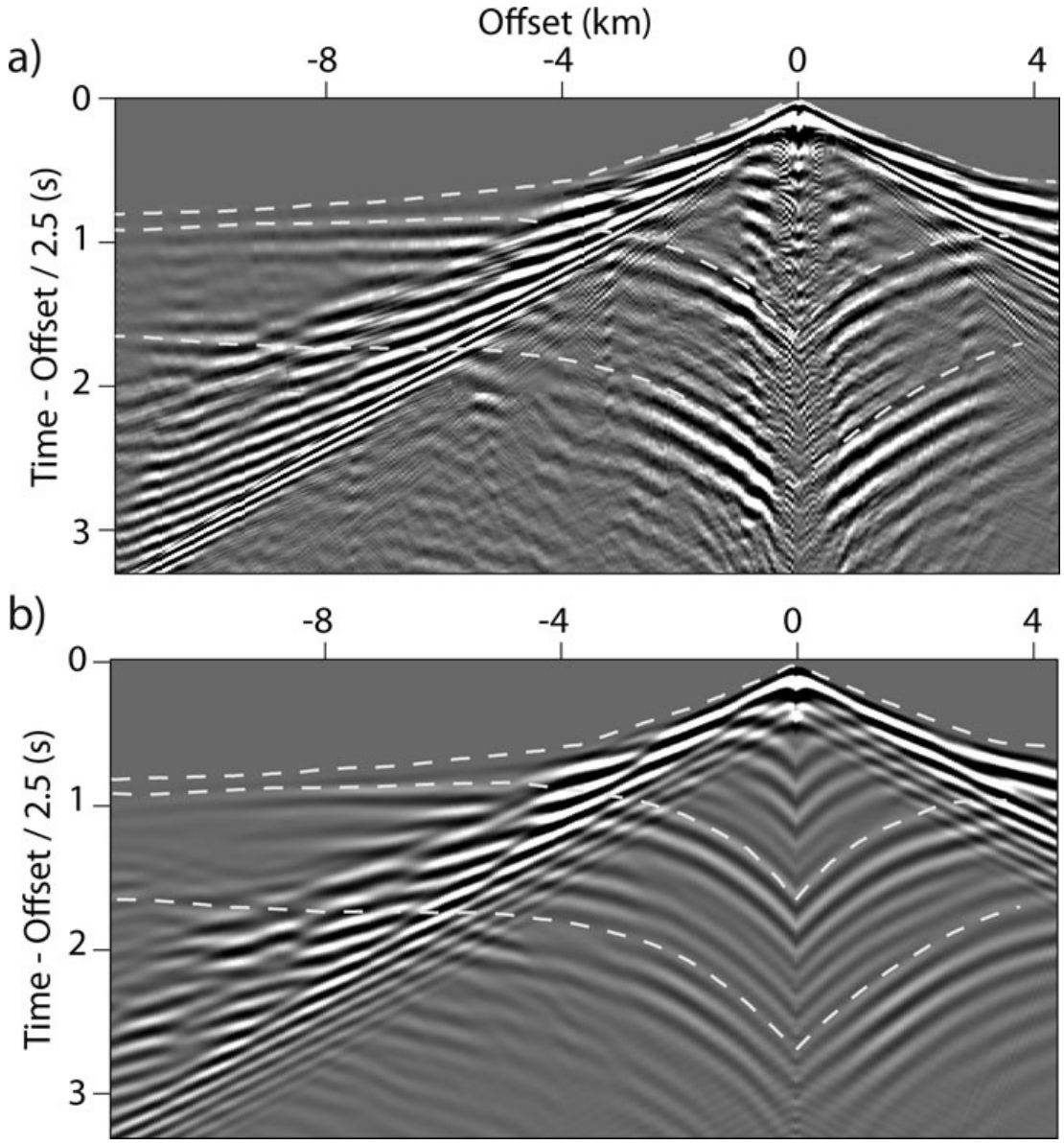

Figure 12. Anisotropic modeling. (a) Recorded receiver gather of Fig. 3(a). (b) Receiver gather computed in the V_0 + FWI model. The dash lines show the first-arrival traveltimes computed in the FATT model and reflection traveltimes for phases Rg and Rr computed in the NMO model.

dominated by the diving waves and long-spread reflections, which sample the first 1.5 km of the medium. As horizontal velocities are reconstructed in the upper structure, this should impact upon the reconstruction of the deep structure that is mainly controlled by short-aperture reflections. Two pieces of evidence relating to this footprint might be low velocities in the gas layers (equal or even lower than the vertical velocities) and the stretching in depth of the velocity structure at the reservoir level. The stretching effect, which is clear in the 3-D FWI results, is well illustrated in the RTM images where the depth of a deep reflector below the reservoir level gradually increases when we move from anisotropic migration to isotropic migration computed in the FATT + FWI models, these latters having the highest velocities in the upper structure. It is worth noting that the trend towards low velocities in the gas and deepening of the reservoir level tends to be strengthened when the pre-whitening factor of the gradient pre-conditioning performed by the diagonal approximate Hessian is relaxed (see also Ravaut *et al.* 2004, their Fig. 15) for the effects of the pre-whitening factor on FWI). This suggests that the low velocities in the gas and the deepening of the top of the reservoir describe a real trend of the FWI convergence for this case study.

Although the 3-D FWI model has been constructed from the NMO velocity model, the 3-D FWI model shares more similarities with the 2-D FATT + FWI models than with the NMO + FWI model. This is clearly shown by both the velocity-depth structure at the well log position (Fig. 7) and by the depths of the reflectors in the RTM images (Figs 8 and 9). This might arise because in 3-D wide-azimuth acquisition, wide-aperture components have a stronger weight in the data than the short-aperture components, compared to 2-D wide-aperture acquisitions.

The third conclusion is related to the ill-posedness of the FWI. We have shown that all of the FWI models provide almost

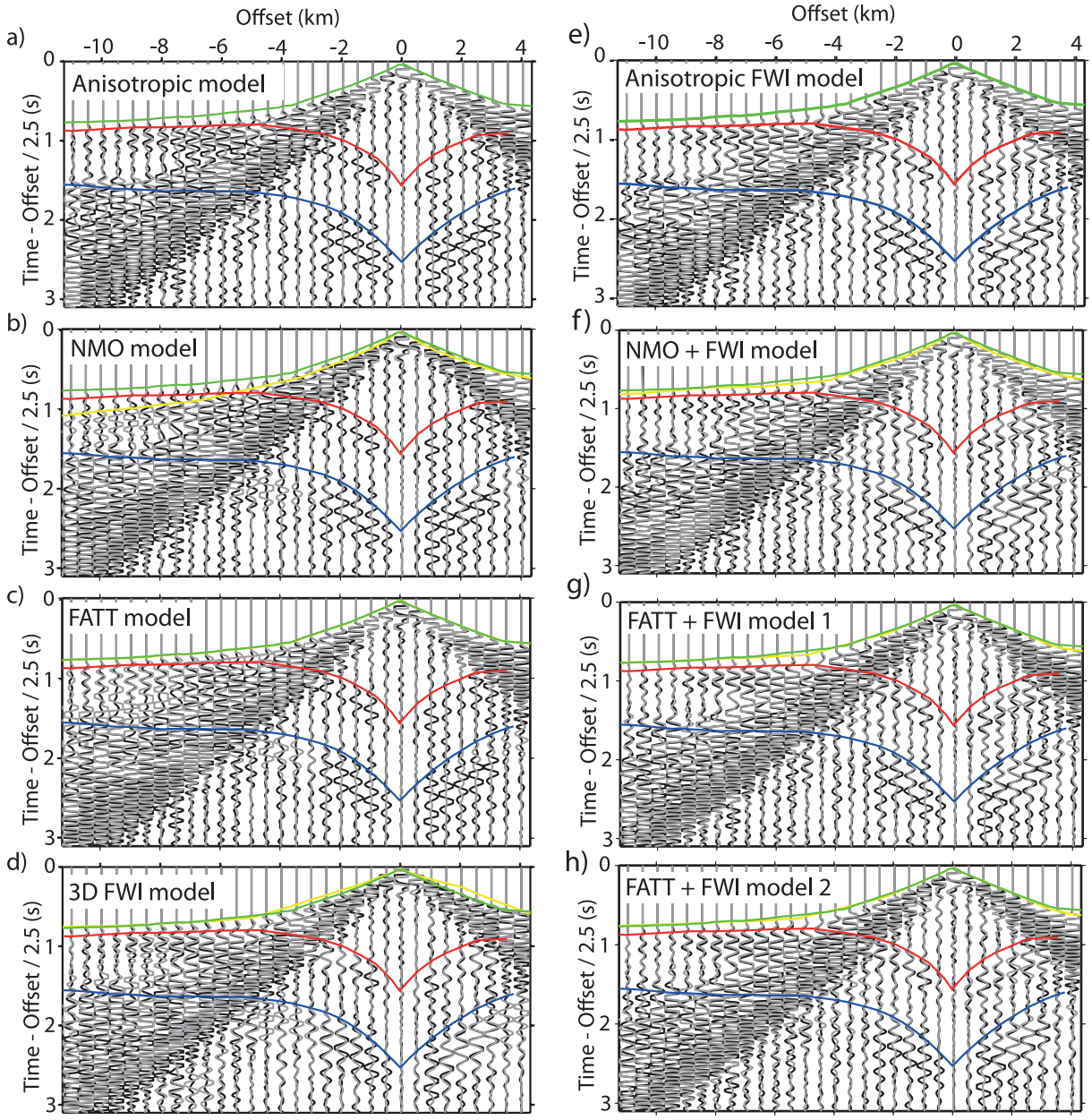

Figure 13. Direct comparison between recorded (black) and modelled (grey) seismograms for the receiver gather of Fig. 3a. (a, e) Anisotropic synthetic seismograms computed in the initial (a) and final (e) (V_0, δ, ϵ) FWI models. (b, f) Isotropic synthetic seismograms computed in the NMO model (b) and in the NMO + FWI model (f). (c,g,h) Isotropic synthetic seismograms computed in the FATT model (c) and in the FATT + FWI models 1 (g) and 2 (h). (d) Isotropic synthetic seismograms computed in the dip section of the 3-D FWI model of Sirgue *et al.* (2010). The green lines denote manually-picked first-arrival traveltimes. The yellow lines denote the computed first-arrival traveltimes in the current model. The red and blue lines are manually-picked reflection traveltimes for the phases Rg and Rr.

equivalent matches of the data at short and wide apertures. Surprisingly, the FWI model inferred from the NMO initial model provides an acceptable match of the waveforms of the diving waves, despite the significant kinematic inaccuracy of the initial NMO velocities at wide apertures. The equivalent ability of the isotropic and anisotropic FWI models to match the data is also highlighted by the similarities of the source wavelet inferred from each FWI model. This raises the difficult issue of anisotropic acoustic FWI where several classes of anisotropic parameters should be reconstructed. Plessix & Cao (2011) and Gholami *et al.* (2011b) concluded that only two anisotropic parameters, related to the either the vertical or the NMO velocity and the horizontal velocity, can be reconstructed. Further demonstrations with realistic synthetic and real data examples need to be performed (Gholami *et al.* 2011a). This will be the aim of future studies.

This study also illustrates that reflection data alone are not suitable for building horizontal velocities in anisotropic media. We first show that the VTI model built by reflection tomography of short-spread reflection data does not match very accurately the first-arrival traveltimes in particular at short and intermediate offsets (Fig. 3b). The accuracy of the anisotropic velocity model in the shallow part is further improved by FWI, which contributes to flatten the CIGs in the shallow part of the medium (Fig. 10). Therefore, combining anisotropic refraction and reflection tomography should provide a

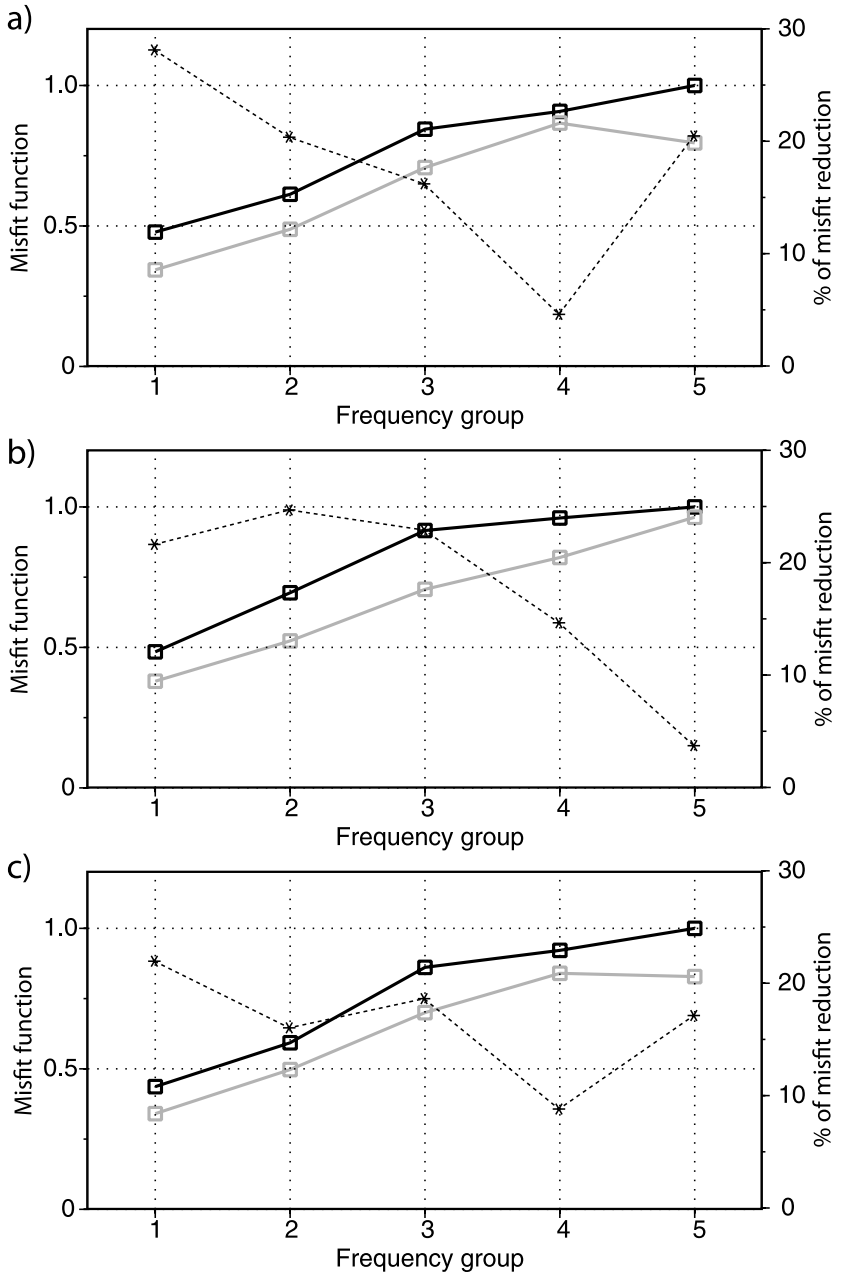

Figure 14. Misfit function at first (solid grey) and last (solid black) iterations versus frequency groups for the anisotropic FWI for V_0 (a), the isotropic FWI using the NMO (b) and the FATT (test 3) (c) model as initial models. The dash line represents the percentage of misfit reduction.

more suitable framework to build an accurate initial model for FWI from wide-aperture data. Extension of anisotropic stereotomography to the joint inversion of refraction and reflection traveltimes is one possible approach to achieve this goal (Prieux *et al.* 2010).

CONCLUSION

The case study of isotropic FWI of the anisotropic wide-aperture data presented in this study has highlighted the footprint of anisotropy on isotropic FWI. We have used a surface real-data case study to discuss the validity of the isotropic approximation to perform FWI of wide-aperture/wide-azimuth data. For these acquisitions, when the data are modelled in the isotropic approximation, the differences between the horizontal and the vertical velocities leads to kinematic inconsistencies between the short-aperture and the wide-aperture components of the data. We show that the isotropic inversion is steered towards the reconstruction of the horizontal velocities in the upper part of the structure, which is sampled by diving waves and long-spread reflections. The reconstruction of the horizontal velocities in the upper structure leads to kinematic inconsistencies during the inversion of the short-spread reflections from deep reflectors, which are mainly sensitive to the vertical and the normal moveout velocities. These kinematic inconsistencies are accommodated by underestimated velocities and/or stretching in depth of the deep structure. Therefore, anisotropy should be involved in FWI to avoid this bias in the velocity estimation and in the depth positioning of the reflectors. Indeed, this is not a trivial task. We have shown how significantly different velocity models allow for a nearly

equivalent match of the data. This highlights the ill-posedness of multiparameter acoustic anisotropic FWI. Therefore, future work will require a careful sensitivity analysis of the anisotropic FWI to define the number and type of parameter classes that can be reliably reconstructed by anisotropic FWI of wide-aperture data, as well as to design efficient strategies to constrain the inversion with suitable prior information coming from well logs.

ACKNOWLEDGMENTS

This study was funded by the SEISCOPE consortium http://seiscope.oca.eu, sponsored by BP, CGG-VERITAS, ENI, EXXON-MOBIL, SAUDI ARAMCO, SHELL, STATOIL and TOTAL. The linear systems were solved with the MUMPS package, which is available on http://graal.ens-lyon.fr/MUMPS/index.html. The mesh generation was performed with the help of TRIANGLE, which is available on http://www.cs.cmu.edu/∼quake/triangle.html. This study was granted access to the high-performance computing facilities of the SIGAMM (Observatoire de la Côte d'Azur) and to the HPC resources of [CINES/IDRIS] under the allocation 2010-[project gao2280] made by GENCI (Grand Equipement National de Calcul Intensif). We gratefully acknowledge both of these Facilities and the support of their staff. We thank BP Norge and Hess Norge for providing us the 2-D raw Valhall data set as well as the data set pre-processed by PGS for migration, the initial anisotropic models, the well log velocities and the 2-D section of the 3-D FWI model of Sirgue *et al.* (2010). We would like to thank the associated Editor, Jeannot Trampert, an anonymous reviewer and R.-E. Plessix, for their very constructive comments.

REFERENCES

Alkhalifah, T. & Tsvankin, I., 1995. Velocity analysis for transversely isotropic media, *Geophysics,* **60,** 1550–1566.

Barnes, C. & Charara, M., 2009. The domain of applicability of acoustic full-waveform inversion for marine seismic data, *Geophysics,* **74,** WCC91–WCC103.

Berenger, J.-P., 1994. A perfectly matched layer for absorption of electromagnetic waves, *J. Comput. Phys.,* **114,** 185–200.

Bleibinhaus, F., Hole, J.A., Ryberg, T. & Fuis, G.S., 2007. Structure of the California Coast Ranges and San Andreas Fault at SAFOD from seismic waveform inversion and reflection imaging, *J. geophys. Res.,* **112,** doi:10.1029/2006JB004611.

Brenders, A.J. & Pratt, R.G., 2007. Full waveform tomography for lithospheric imaging: results from a blind test in a realistic crustal model, *Geophys. J. Int.,* **168,** 133–151.

Brossier, R., 2011. Two-dimensional frequency-domain visco-elastic full waveform inversion: parallel algorithms, optimization and performance, *Comput. Geosci.,* **37,** 444–455.

Brossier, R. & Roux, P., 2011. Seismic imaging by frequency-domain double-beamforming full-waveform inversion, *73rd EAGE Conference & Exhibition*, available at http://www.earthdoc.org/detail.php?pubid=50200.

Brossier, R., Virieux, J. & Operto, S., 2008. Parsimonious finite-volume frequency-domain method for 2-D P-SV-wave modelling, *Geophys. J. Int.,* **175,** 541–559.

Brossier, R., Operto, S. & Virieux, J., 2009a. Seismic imaging of complex onshore structures by 2D elastic frequency-domain full-waveform inversion, *Geophysics,* **74,** WCC63–WCC76.

Brossier, R., Operto, S. & Virieux, J., 2009b. Two-dimensional seismic imaging of the Valhall model from synthetic OBC data by frequency-domain elastic full-waveform inversion, *SEG Expanded Abstracts,* **28,** 2293–2297.

Brossier, R., Gholami, Y., Virieux, J. & Operto, S., 2010a. 2D frequency-domain seismic wave modeling in VTI media based on a Hp-adaptive discontinuous Galerkin method, *72nd EAGE Conference & Exhibition*, available at http://www.earthdoc.org/detail.php?pubid=39193.

Brossier, R., Operto, S. & Virieux, J., 2010b. Which data residual norm for robust elastic frequency-domain full waveform inversion?, *Geophysics,* **75,** R37–R46.

Bunks, C., Salek, F.M., Zaleski, S. & Chavent, G., 1995. Multiscale seismic waveform inversion, *Geophysics,* **60,** 1457–1473.

Chavent, G., 2009. *Nonlinear Least Squares for Inverse Problems*, Springer, Dordrecht.

Gardner, G.H.F., Gardner, L.W. & Gregory, A.R., 1974. Formation velocity and density—the diagnostic basics for stratigraphic traps, *Geophysics,* **39,** 770–780.

Gauthier, O., Virieux, J. & Tarantola, A., 1986. Two-dimensional nonlinear inversion of seismic waveforms: numerical results, *Geophysics,* **51,** 1387–1403.

Gholami, Y., Brossier, R., Operto, S., Prieux, V., Ribodetti, A. & Virieux, J., 2011a. Two-dimensional acoustic anisotropic (VTI) full waveform inversion: the Valhall case study, *SEG Expanded Abstracts*, **30,** 2543.

Gholami, Y., Brossier, R., Operto, S., Ribodetti, A. & Virieux, J., 2011b. Acoustic anisotropic full waveform inversion: sensitivity analysis and realistic synthetic examples, *SEG Expanded Abstracts*, **30,** 2465.

Gouveia, W.P. & Scales, J.A., 1998. Bayesian seismic waveform inversion: parameter estimation and uncertainty analysis, *J. geophys. Res.,* **103,** 2579–2779.

Guitton, A., Ayeni, G. & Gonzales, G., 2010. A preconditioning scheme for full waveform inversion, *SEG Expanded Abstracts,* **29,** 1008–1012.

Jaiswal, P., Zelt, C., Dasgupta, R. & Nath, K., 2009. Seismic imaging of the Naga Thrust using multiscale waveform inversion, *Geophysics,* **74**(6), WCC129–WCC140.

Kommedal, J.H., Barkved, O.I. & Howe, D.J., 2004. Initial experience operating a permanent 4C seabed array for reservoir monitoring at Valhall, *SEG Expanded Abstracts,* **23,** 2239–2242.

Kommedal, J.H., Barkved, O.I. & Thomsen, L.A., 1997. Acquisition of 4 component obs data—a case study from the Valhall field, *59th EAGE Conference & Exhibition*, available at http://www.earthdoc.org/detail.php?pubid=24627.

Lee, H.-Y., Koo, J.M., Min, D.-J., Kwon, B.-D. & Yoo, H.S., 2010. Frequency-domain elastic full-waveform inversion for VTI media, *Geophys. J. Int.,* **183,** 884–904.

Mari, J.L., Glangeaud, F. & Coppens, F., 1999. *Signal Processing for Geologists & Geophysicists*, Institut Français du Pétrole Publications, Editions Technip, Paris, 480pp.

Mora, P.R., 1987. Nonlinear two-dimensional elastic inversion of multi-offset seismic data, *Geophysics,* **52,** 1211–1228.

Mora, P.R., 1988. Elastic wavefield inversion of reflection and transmission data, *Geophysics,* **53,** 750–759.

MUMPS-team, 2009. *MUMPS - MUltifrontal Massively Parallel Solver Users' Guide - Version 4.9.2*, ENSEEIHT-ENS Lyon, available at http://www.enseeiht.fr/apo/MUMPS/ or http://graal.ens-lyon.fr/MUMPS (last accessed 2009 November 5).

Munns, J.W., 1985. The Valhall field: a geological overview, *Mar. Petrol. Geol.,* **2,** 23–43.

Neves, F.A. & Singh, S.C., 1996. Sensitivity study of seismic reflection/refraction data, *Geophys. J. Int.,* **126,** 470–476.

Operto, S., Virieux, J., Dessa, J.X. & Pascal, G., 2006. Crustal imaging from multifold ocean bottom seismometers data by frequency-domain full-waveform tomography: application to the eastern Nankai trough, *J. geophys. Res.,* **111,** B09306, doi:10.1029/2005JB003835.

Operto, S., Virieux, J., Ribodetti, A. & Anderson, J.E., 2009. Finite-difference frequency-domain modeling of visco-acoustic wave propagation in two-dimensional TTI media, *Geophysics,* **74**(5), T75–T95.

Plessix, R.-E., 2006. A review of the adjoint-state method for computing the gradient of a functional with geophysical applications, *Geophys. J. Int.,* **167,** 495–503.

Plessix, R.-E., 2009. Three-dimensional frequency-domain full-waveform inversion with an iterative solver, *Geophysics,* **74,** WCC53–WCC61.

Plessix, R.-E., Baeten, G., de Maag, J.W., Klaassen, M., Rujie, Z. & Zhifei, T., 2010. Application of acoustic full waveform inversion to a

low-frequency large-offset land data set, *SEG Expanded Abstracts,* **29,** 930–934.

Plessix, R.E. & Perkins, C., 2010. Full waveform inversion of a deep water ocean bottom seismometer dataset, *First Break,* **28,** 71–78.

Plessix, R.E. & Cao, Q., 2011. A parameterization study for surface seismic full waveform inversion in an acoustic vertical transversely isotropic medium, *Geophys. J. Int.,* **185,** 539–556.

Podvin, P. & Lecomte, I., 1991. Finite difference computation of traveltimes in very contrasted velocity model: a massively parallel approach and its associated tools, *Geophys. J. Int.,* **105,** 271–284.

Polak, E. & Ribière, G., 1969. Note sur la convergence de méthodes de directions conjuguées, *Revue Française d'Informatique et de Recherche Opérationnelle*, **16,** 35–43.

Pratt, R.G., 1999. Seismic waveform inversion in the frequency domain, Part I: theory and verification in a physic scale model, *Geophysics,* **64,** 888–901.

Pratt, R.G., 2008. Waveform tomography—successes, cautionary tales, and future directions, *70th EAGE Conference & Exhibition*, available at http://www.earthdoc.org/detail.php?pubid=9827.

Pratt, R.G. & Worthington, M.H., 1990. Inverse theory applied to multi-source cross-hole tomography. Part I: acoustic wave-equation method, *Geophys. Prospect.,* **38,** 287–310.

Pratt, R.G. & Sams, M.S., 1996. Reconciliation of crosshole seismic velocities with well information in a layered sedimentary environment, *Geophysics,* **61,** 549–560.

Pratt, R.G. & Shipp, R.M., 1999. Seismic waveform inversion in the frequency domain, Part II: Fault delineation in sediments using crosshole data, *Geophysics,* **64,** 902–914.

Pratt, R.G., Shin, C. & Hicks, G.J., 1998. Gauss-Newton and full Newton methods in frequency-space seismic waveform inversion, *Geophys. J. Int.,* **133,** 341–362.

Pratt, R.G., Plessix, R.E. & Mulder, W.A., 2001. Seismic waveform tomography: the effect of layering and anisotropy, *63rd EAGE Conference & Exhibition*, available at http://www.earthdoc.org/detail.php?pubid=4414.

Pratt, R.G., Song, Z.M. & Warner, M., 1996. Two-dimensional velocity models from wide angle seismic data by wavefield inversion, *Geophys. J. Int.,* **124,** 323–340.

Prieux, V., Operto, S., Lambaré G. & Virieux, J., 2010. Building starting model for full waveform inversion from wide aperture data by stereotomography, *SEG Expanded Abstracts,* **29,** 988–992.

Ravaut, C., Operto, S., Improta, L., Virieux, J., Herrero, A. & dell'Aversana, P., 2004. Multi-scale imaging of complex structures from multi-fold wide aperture seismic data by frequency-domain full-wavefield inversions: application to a thrust belt, *Geophys. J. Int.,* **159,** 1032–1056.

Robertson, J.O.A., Holliger, K., Green, A.G., Pugin, A. & Iaco, R.D., 1996. Effects of near-surface waveguides on shallow high-resolution seismic refraction and reflection data, *Geophys. Res. Lett.,* **23,** 495–498.

Sheng, J., Leeds, A., Buddensiek, M. & Schuster, G.T., 2006. Early arrival waveform tomography on near-surface refraction data, *Geophysics,* **71**(4), U47–U57.

Shin, C. & Ha, Y.H., 2009. Waveform inversion in the Laplace-Fourier domain, *Geophys. J. Int.,* **177,** 1067–1079.

Shipp, R.M. & Singh, S.C., 2002. Two-dimensional full wavefield inversion of wide aperture marine seismic streamer data, *Geophys. J. Int.,* **151,** 325–344.

Sirgue, L., 2006. The importance of low frequency and large offset in waveform inversion, *68th EAGE Conference & Exhibition*, available at http://www.earthdoc.org/detail.php?pubid=187.

Sirgue, L. & Pratt, R.G., 2004. Efficient waveform inversion and imaging: a strategy for selecting temporal frequencies, *Geophysics,* **69,** 231–248.

Sirgue, L., Barkved, O.I., Dellinger, J., Etgen, J., Albertin, U. & Kommedal, J.H., 2010. Full waveform inversion: the next leap forward in imaging at Valhall, *First Break,* **28,** 65–70.

Sirgue, L., Barkved, O.I., Gestel, J.P.V., Askim, O.J. & Kommedal, J.H., 2009. 3D waveform inversion on Valhall wide azimuth OBC, *71st EAGE Conference & Exhibition*, available at http://www.earthdoc.org/detail.php?pubid=24070.

Sourbier, F., Operto, S., Virieux, J., Amestoy, P. & L'Excellent, J.-Y., 2009a. Fwt2d: A massively parallel program for frequency-domain full-waveform tomography of wide aperture seismic data—part 1: algorithm, *Comput. Geosci.,* **35,** 487–495.

Sourbier, F., Operto, S., Virieux, J., Amestoy, P. & L'Excellent, J.-Y., 2009b. Fwt2d: a massively parallel program for frequency-domain full-waveform tomography of wide aperture seismic data–part 2: numerical examples and scalability analysis, *Comput. Geosci.,* **35,** 496–514.

Symes, W.W., 2008. Migration velocity analysis and waveform inversion, *Geophys. Prospect.,* **56,** 765–790.

Tarantola, A., 2005. *Inverse Problem Theory and Methods for Model Parameter Estimation*, SIAM, Philadelphia, PA.

Thomsen, L.A., 1986. Weak elastic anisotropy, *Geophysics,* **51,** 1954–1966.

Tsvankin, I., 1995. Normal moveout from dipping reflectors in anisotropic media, *Geophysics,* **60,** 268–284.

Tsvankin, I., 2001. Seismic signature and analysis of reflection data in anisotropic media, *Seismic Exploration*, Handbook of Geophysical Exploration Vol. 29, eds. Helbig, K. & Treitel, S., Pergamon Press, Oxford.

Vigh, D., Starr, B., Kapoor, J. & Li, H., 2010. 3d full waveform inversion on a Gulf of Mexico Waz data set, *SEG Technical Program Expanded Abstracts,* **29,** 957–961.

Virieux, J. & Operto, S., 2009. An overview of full waveform inversion in exploration geophysics, *Geophysics,* **74**(6), WCC127–WCC152.

Wang, Y. & Rao, Y., 2009. Reflection seismic waveform tomography, *J. geophys. Res.,* **114,** doi:10.1029/2008JB005916.